

Examining CO₂ model observation residuals and their implications for carbon fluxes and transport using ACT-America observations

Tobias Gerken¹, Sha Feng², Klaus Keller³, Thomas Lauvaux⁴, Joshua P. Digangi⁵, Yonghoon Choi⁵, Bianca Baier⁶, and Kenneth J Davis³

¹James Madison University

²Pacific Northwest National Lab

³The Pennsylvania State University

⁴LSCE IPSL

⁵NASA Langley Research Center

⁶University of Colorado-Boulder

November 21, 2022

Abstract

Atmospheric CO₂ inversion typically relies on the specification of prior flux and atmospheric model transport errors, which have large uncertainties. Here, we use ACT-America 30 airborne observations to compare total CO₂ model-observation mismatch in the eastern U.S. and during four climatological seasons for the mesoscale WRF(-Chem) and global scale CarbonTracker/TM5 (CT) models. Models used identical surface carbon fluxes, and CT was used as CO₂ boundary condition for WRF. Both models show reasonable agreement with observations, and CO₂ residuals follow near symmetric peaked (i.e. non-Gaussian) distribution with near zero bias of both models (CT: -0.34 +/- 3.12 ppm; WRF: 0.82 +/- 4.37 ppm). We also encountered large magnitude residuals at the tails of the distribution that contribute considerably to overall bias. Atmospheric boundary-layer biases (1-10 ppm) were much larger than free tropospheric biases (0.5-1 ppm) and were of same magnitude as model-model differences, whereas free tropospheric biases were mostly governed by CO₂ background conditions. Results revealed systematic differences in atmospheric transport, most pronounced in the warm and cold sectors of synoptic systems, highlighting the importance of transport for CO₂ residuals. While CT could reproduce the principal CO₂ dynamics associated with synoptic systems, WRF showed a clearer distinction for CO₂ differences across fronts. Variograms were used to quantify spatial coherence of residuals and showed characteristic residual length scales of approximately 100 km to 300 km. Our findings suggest that inclusion of synoptic weather-dependent and non-Gaussian error structure may benefit inversion systems.

1 **Examining CO₂ model observation residuals and their**
2 **implications for carbon fluxes and transport using**
3 **ACT-America observations**

4 **Tobias Gerken^{1,*}, Sha Feng^{1,**}, Klaus Keller^{2,3}, Thomas Lauvaux⁴, Joshua P.**
5 **DiGangi⁵, Yonghoon Choi^{5,6}, Bianca Baier^{7,8}, Kenneth J. Davis^{1,3}**

6 ¹Department of Meteorology and Atmospheric Science, The Pennsylvania State University, University
7 Park, PA 16802, USA

8 ²Department of Geosciences, The Pennsylvania State University, University Park, PA 16802, USA

9 ³Earth and Environmental Systems Institute, The Pennsylvania State University, University Park, PA
10 16802, USA

11 ⁴Laboratoire des Sciences du Climat et de l'Environnement, CEA, CNRS, UVSQ/IPSL, Université
12 Paris-Saclay, Orme des Merisiers, 91191 Gif-sur-Yvette CEDEX, France

13 ⁵NASA Langley Research Center, Hampton, VA 2368, USA

14 ⁶Science Systems and Applications Inc., Hampton, VA 23681, USA

15 ⁷Cooperative Institute for Research in Environmental Sciences, University of Colorado-Boulder, Boulder,
16 CO 80309, USA

17 ⁸NOAA Global Monitoring Laboratory, Boulder, CO 80305, USA

18 *Now at: School of Integrated Sciences, James Madison University, Harrisonburg, VA 22807, USA

19 **Now at: Atmospheric Sciences & Global Change Division, Pacific Northwest National Laboratory,
20 Richland, WA 99354, USA

21 **Key Points:**

- 22 • CO₂ observed by aircraft in Eastern U.S. compares well to models, but residuals
23 are strongly non-Gaussian.
- 24 • Model biases affect representation of cross-frontal CO₂ gradients governing CO₂
25 transport in storms.
- 26 • Inversion models may benefit from model-data mismatch errors dependent upon
27 synoptic sector.

Corresponding author: Tobias Gerken, gerkentx@jmu.edu

Abstract

28 Atmospheric CO₂ inversion typically relies on the specification of prior flux and atmo-
29 spheric model transport errors, which have large uncertainties. Here, we use ACT-America
30 airborne observations to compare total CO₂ model-observation mismatch in the east-
31 ern U.S. and during four climatological seasons for the mesoscale WRF(-Chem) and global
32 scale CarbonTracker/TM5 (CT) models. Models used identical surface carbon fluxes,
33 and CT was used as CO₂ boundary condition for WRF. Both models show reasonable
34 agreement with observations, and CO₂ residuals follow near symmetric peaked (i.e. non-
35 Gaussian) distribution with near zero bias of both models (CT: -0.34 ± 3.12 ppm; WRF:
36 0.82 ± 4.37 ppm). We also encountered large magnitude residuals at the tails of the dis-
37 tribution that contribute considerably to overall bias. Atmospheric boundary-layer bi-
38 ases (1–10 ppm) were much larger than free tropospheric biases (0.5–1 ppm) and were
39 of same magnitude as model-model differences, whereas free tropospheric biases were mostly
40 governed by CO₂ background conditions. Results revealed systematic differences in at-
41 mospheric transport, most pronounced in the warm and cold sectors of synoptic systems,
42 highlighting the importance of transport for CO₂ residuals. While CT could reproduce
43 the principal CO₂ dynamics associated with synoptic systems, WRF showed a clearer
44 distinction for CO₂ differences across fronts. Variograms were used to quantify spatial
45 coherence of residuals and showed characteristic residual length scales of approximately
46 100 km to 300 km. Our findings suggest that inclusion of synoptic weather-dependent and
47 non-Gaussian error structure may benefit inversion systems.
48

1 Introduction

49
50 To understand ongoing and future global climate change, it is necessary to improve
51 our understanding of the terrestrial carbon cycle. Increasing atmospheric CO₂ concen-
52 trations from the combustion of fossil fuels and land-use change are partially balanced
53 by carbon uptake in the terrestrial biosphere (Myhre et al., 2013). While the global car-
54 bon budget is constrained to a reasonable degree (Ciais et al., 2013), regional sources
55 and sinks (Peylin et al., 2013; Crowell et al., 2019) as well as future trends (Friedlingstein
56 et al., 2014) are much less well understood and cannot be easily diagnosed from terres-
57 trial biosphere models, as they disagree substantially in temporal dynamics and the sign
58 of carbon uptake (Huntzinger et al., 2012).

59 Atmospheric inversion systems provide a *top-down* approach to estimating terres-
60 trial carbon fluxes and a complementary perspective to ecosystem models (Gurney et
61 al., 2002; Bousquet et al., 1999). Most inversion models rely on both prior estimates of
62 ecosystem carbon fluxes and atmospheric transport models to optimize fluxes with re-
63 spect to observed atmospheric CO₂ mole fractions ([CO₂]). They are subject to uncer-
64 tainties arising from limited observations of atmospheric [CO₂], atmospheric model trans-
65 port errors, and uncertain prior flux estimates. Model transport errors in particular are
66 widely considered to be a major source of uncertainty for atmospheric inversion systems
67 (Peylin et al., 2005; Baker et al., 2006; Stephens et al., 2007; Gerbig et al., 2008; Cheval-
68 lier et al., 2010; Lauvaux & Davis, 2014; Díaz-Isaac et al., 2014; Schuh et al., 2019). For
69 example, Stephens et al. (2007) demonstrated the far reaching effects of the atmospheric
70 transport model choice by showing that substantial biases in atmospheric CO₂ gradi-
71 ents (i.e. vertical mixing) resulted in considerable differences in estimated regional fluxes
72 and Peylin et al. (2013) found a large uncertainty in North American terrestrial carbon
73 sink ($0.75 \pm 0.45 \text{ PgC y}^{-1}$) in a comparison of atmospheric inversion systems, highlight-
74 ing the role of transport uncertainty for atmospheric inversion. Uncertainty attributed
75 to transport models appears to be independent of regional sampling density, such that
76 tropical and extratropical regions exhibit similar transport uncertainties (Basu et al., 2018).
77 While additional atmospheric CO₂ observations in the tropics are crucially needed to con-
78 strain regional carbon balances, quantification and reduction of transport uncertainty
79 is a priority for improving flux estimates in North America.

80 With respect to regional inversion systems, it was found that different atmospheric
81 boundary-layer (ABL) parameterizations can cause substantial changes in regional in-
82 verse flux estimates (Lauvaux & Davis, 2014) due to differences in ABL depth and ver-
83 tical mixing strength. Also, all physical parameterizations within one numerical weather
84 model lead to considerable variability in ABL CO₂ (Díaz-Isaac et al., 2018). The impact
85 of atmospheric mixing strength on inversion results is exacerbated by the fact that the
86 CO₂ mass balance in inversion models must be maintained, which then leads to erroneous
87 latitudinal transport of CO₂. Transport uncertainty clearly manifests itself in ABL CO₂
88 mole fractions, and large differences have been found within global and regional atmo-
89 spheric models (e.g. Díaz-Isaac et al., 2018; Chen, Zhang, Lauvaux, et al., 2019; Schuh
90 et al., 2019). At the same time, Gaubert et al. (2019) recently challenged the notion that
91 vertical CO₂ gradients were the dominant cause of uncertainty in the North American

92 carbon sink for current global inversions, and suggested that uncertainties in the fossil
93 fuel prior were responsible.

94 Feng, Lauvaux, Davis, et al. (2019) showed that both fossil fuel fluxes and conti-
95 nental boundary conditions play important roles in the uncertainty in ABL CO₂ in ad-
96 dition to atmospheric transport, but concluded that biogenic fluxes, the typical objec-
97 tive of atmospheric inverse analyses, are the largest source of uncertainty.

98 While atmospheric inversions have been crucial for estimating global to continen-
99 tal scale carbon sources and sinks, limited progress has been made in constraining re-
100 gional carbon fluxes on seasonal scales. The coarse resolution of transport models in global
101 inversion systems (typically 1° × 1° or coarser) may limit their ability to resolve finer
102 scale atmospheric transport in weather systems and complex terrain (Geels et al., 2007).
103 Regional inversions with higher model resolutions, such as CarbonTracker-Lagrange (Hu
104 et al., 2019), have been successfully applied to constrain ecosystem carbon fluxes at re-
105 gional (Lauvaux, Schuh, Bocquet, et al., 2012; Lauvaux, Schuh, Uliasz, et al., 2012; Schuh
106 et al., 2013) and continental (Hu et al., 2019) scales, but rely on high density CO₂ ob-
107 servations as well as the model’s ability to reproduce boundary layer processes and syn-
108 optoc weather systems. Synoptic systems in the northern mid-latitudes are responsible
109 for up to 70% of CO₂ variability through advection and are the dominant mechanism
110 of day to day CO₂ variability in the ABL, and synoptic scale fronts create large contrasts
111 in near surface CO₂ (Parazoo et al., 2008, 2011). Parazoo et al. (2012) highlighted that
112 CO₂ flux estimates were highly sensitive to such synoptic scale gradients.

113 It is therefore desirable that transport models are capable of producing relevant
114 frontal processes such as (i) advection of upstream CO₂ gradients (e.g. Keppel-Aleks et
115 al., 2011, 2012), (ii) moist convective lifting of ABL air and (Schuh et al., 2019) (iii) mod-
116 ification of ecosystem CO₂ exchange due to weather effects (e.g. Chan et al., 2004). Com-
117 paring global inversion system’s ABL dynamics, vertical mixing, and convection at frontal
118 boundaries were also identified as priorities for improving CO₂ flux estimates in the north-
119 ern mid-latitudes (Schuh et al., 2019).

120 The CarbonTracker (Peters et al., 2007) global inversion modeling system uses the
121 Transport Model Version 5 (TM5) atmospheric model (Krol et al., 2005) with ECMWF
122 (European Centre for Medium Range Weather Forecasting) ERA-Interim reanalysis me-
123 teorological drivers to estimate surface fluxes of CO₂. TM5’s spatial resolution above North

124 America is $1^\circ \times 1^\circ$. CarbonTracker ingests a variety of global CO₂ data sources includ-
125 ing daily flask observations, hourly surface time series data, and aircraft observations (Andrews
126 et al., 2014; Sweeney et al., 2015) and can be used as a reference point for inversion
127 systems.

128 The NASA funded Atmospheric Carbon and Transport (ACT) -America Earth Ven-
129 ture Suborbital Mission was designed to observe atmospheric CO₂ and CH₄ mole frac-
130 tions in the central and eastern United States, the dominant region for North American
131 ecosystem CO₂ fluxes and atmospheric [CO₂] variability, and provide the observational
132 basis for improving regional flux inversions in this region and across the midlatitudes.
133 The ecosystem fluxes, atmospheric CO₂ mole fractions (Sweeney et al., 2015) and weather
134 patterns all exhibit strong seasonal variability (e.g. Merrill & Moody, 1996). ACT-America
135 sampled atmospheric CO₂ and CH₄ and associated weather variables across (i) multi-
136 ple altitudes, (ii) fair weather and frontal conditions (including cross-frontal differences),
137 (iii) multiple regions, and (iv) all four meteorological seasons within the scope of five,
138 six-week flight campaigns. ACT-America provides an ideal test-bed for exploring the abil-
139 ity of atmospheric models to simulate atmospheric CO₂ across weather systems typical
140 of the central and eastern United States, and thus shed light on both global and regional
141 atmospheric inversion system behavior.

142 In this work, we compare atmospheric CO₂ model-observation differences between
143 ACT-America data using both the global CarbonTracker inversion system and the mesoscale
144 Weather Research and Forecasting model (Skamarock et al., 2008) coupled with chem-
145 istry, commonly known as WRF-Chem, which was run for the ACT-America study do-
146 main using CarbonTracker surface carbon fluxes and lateral boundary conditions. For sim-
147 plicity, we use WRF throughout this paper, when referring to WRF-Chem and CT when
148 referring to the specific CarbonTracker-data used in this work (see Methods). Carbon-
149 Tracker is used when we refer to the overall inversion system. This experiment thus fo-
150 cuses on how these two different transport systems represent atmospheric CO₂ with re-
151 spect to the ACT observations given the same fluxes.

152 We analyze the properties of CO₂ model-observation differences along flight tracks
153 and establish a baseline and general approach for comparing mesoscale (WRF) and con-
154 tinental scale (CarbonTracker) model errors, which can be further extended to other at-
155 mospheric inversion (e.g. CarbonTracker-Lagrange) or regional modeling systems. Model-

156 data residuals are investigated as a function of region, altitude, climatological season,
157 and airmass associated with frontal structure. These analyses – and the frontal analy-
158 sis in particular – enable a comparison of the mesoscale and continental scale models for
159 atmospheric conditions that are important to CO₂ transport. At the same time, these
160 synoptically active conditions are often avoided in airborne networks such as the NOAA
161 CCGG (Carbon Cycle and Greenhouse Gases) Aircraft Program (Sweeney et al., 2015)
162 and partially hidden from satellite remote sensing due to cloud interference (e.g. Para-
163 zoo et al., 2008).

164 This paper investigates total model-data mismatch; our results are intended to guide
165 future diagnostic studies that will separate flux and transport errors.

166 2 Materials and Methods

167 2.1 ACT-America aircraft observations

168 This work uses 5 s averaged aircraft CO₂ dry mole fractions measured using a PI-
169 CARRO G2401-m cavity ring down spectrometer and [CO₂] calibration is traceable to
170 X2007-scale. Data are published as part of the *ACT-America: L3 Merged In Situ At-*
171 *mospheric Trace Gases and Flask Data, Eastern USA* dataset (Update: 2019-03-04) (Davis
172 et al., 2018), which is freely available from the Oak Ridge National Lab Distributed Archive
173 Center (ORNL DAAC) (Wei et al., in review). The NASA Langley Beechcraft B-200 King
174 Air and the NASA Goddard Space Flight Center’s C-130H aircraft were used to collect
175 high quality insitu and remote sensing measurements across the Eastern United States.
176 Given the average speed of the aircraft (100 and 120 m s⁻¹, respectively), the 5 s aver-
177 aged aircraft observations have a spatial resolution of 500-600 m (Chen, Zhang, Lauvaux,
178 et al., 2019). Data used in this work were collected during four intensive observation pe-
179 riod flight campaigns aligning approximately with climatological seasons. We use these
180 campaigns as proxies for seasonal greenhouse gas behavior.

181 During each of the flight campaigns aircraft were operated from 3 different bases
182 (Wallops/Norfolk, Virginia; Lincoln, Nebraska; Shreveport, Louisiana), which approx-
183 imately correspond to study domains (Table 1) referred to as NorthEast Mid-Atlantic
184 (NEMA), Mid-West (MW), and South Central (SC) U.S. We are using geographic co-
185 ordinates of individual measurement locations to delineate flight regions. The South Cen-
186 tral U.S. are defined as flights as Texas, Oklahoma, and the area south of latitude N 37.00°

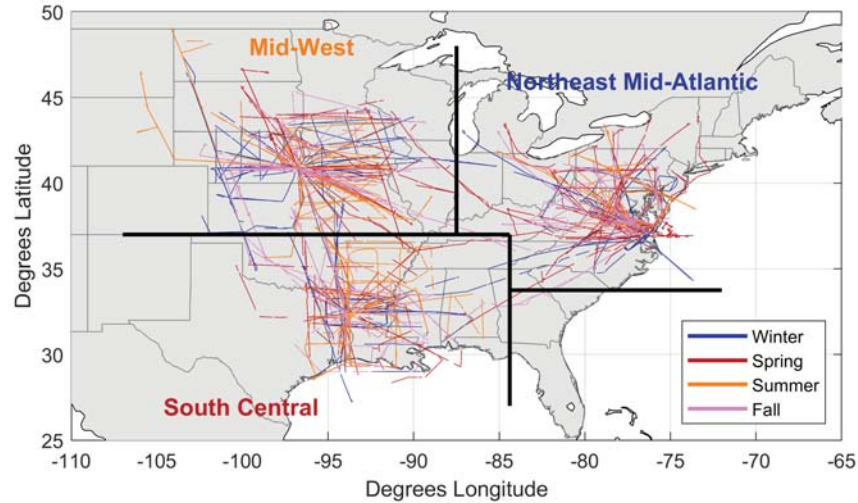


Figure 1. Overview of ACT-America observation data considered in this work. Colored lines indicate level-leg flight tracks by campaign. Study sub-regions as outlined in text are also indicated.

187 (Latitude of the Oklahoma-Kansas border) as well as west of longitude E 84.39° (Lon-
 188 gitude of the city of Atlanta). The Mid-West U.S. region is defined as the area north of
 189 N 37.00° and west of E 87.5° (Longitude of the Illinois-Indiana border) and extending
 190 south to N 33.75° (Latitude of Atlanta), but excluding the area previously defined as South
 191 Central. The geographic distribution of flight observations used in this work is displayed
 192 in Figure 1.

193 We divide aircraft data into three altitude classes which roughly correspond to the
 194 atmospheric boundary-layer (<1.5 km; all altitudes in above ground level), the lower free
 195 troposphere that is frequently affected by convective clouds and mixing (≥ 1.5 to <4.0 km;
 196 LFT), and higher free troposphere which is less often affected by convection and thus
 197 might be akin to background conditions (≥ 4 km) (Sweeney et al., 2015; Baier et al., 2020).
 198 Flight planning during the ACT-America campaign was cognizant of these altitude classes.
 199 For example, despite large diurnal and seasonal variability of ABL-heights, ACT-America
 200 flight legs below 1.5 km altitude attempted to stay within the ABL by maintaining, when-
 201 ever possible, a flight altitude of 330 m AGL. The next level is altitude was specifically

202 selected to be above the ABL, depending on forecasts and ABL depths observed in flight.
203 To reduce mis-classification of vertical levels, we confined our analysis to flight segments
204 that were classified as level-legs, meaning without considerable (>500 m) flight altitude
205 changes indicative of either vertical profiling or maneuvers to evade clouds during visual
206 flight rules, as defined in the ACT-America maneuver flag product produced by the *ACT_ManeuverFlags*
207 algorithm Version 1.0 (Gerken, 2019).

208 Additionally, ACT observations are classified by airmass conditions. Flights were
209 planned to sample synoptic systems by flying cross-frontal transects through cold and
210 warm sectors of the system. Similarly, fair weather flights were planned to sample fair
211 weather conditions as well as pre-frontal warm airmasses and post-frontal cold airmasses.
212 During days when no frontal crossings were flown, all data were either attributed to cold/
213 warm airmasses or fair conditions depending flight location with respect to the synop-
214 tic systems as indicated by National Weather Service surface analysis maps. During flights
215 when fronts (typically cold fronts) were crossed, data flags were manually assigned to
216 separate flights into warm and cold airmasses based on equivalent potential temperature
217 (θ_e), wind, and trace gas changes across fronts. Airmass flags and flight type flags are
218 published on the ONRL DAAC as part of the ACT L3 merged data set (Davis et al., 2018).
219 ACT research flights were typically conducted from local time mid-morning – i.e. after
220 the development of a sufficiently deep convective ABL for aircraft operation within the
221 ABL – to late afternoon, corresponding to range of the C-130 aircraft and to avoid night-
222 time conditions and collapsed ABLs.

223 **2.1.1 CarbonTracker**

224 We use total posterior atmospheric [CO₂] from NOAA’s CarbonTracker (Peters et
225 al., 2007, with updates documented at <http://carbontracker.noaa.gov>) available from the
226 NOAA Global Monitoring Laboratory. Given that our ACT-America research period spans
227 the years from 2016 to 2018, the CT2017 release is used for the summer 2016 campaign,
228 while other seasons use the CT-NRT.v2019-2 (CarbonTracker – Near-Real Time). CT-
229 NRT, designed to extend CarbonTracker between official releases, employs the same TM5
230 atmospheric model, while assimilating a smaller subset of [CO₂] observations. Similarly,
231 real-time meteorology and a simplified terrestrial ecosystem carbon flux prior are being
232 used for CT-NRT. A recent two-season comparison between CT-NRT and ACT aircraft
233 observations found overall reasonable agreement between modeled and observed [CO₂],

Table 1. ACT-America Aircraft Campaigns

Campaign	Region	Start & End Dates	# Flight Days ^a
Summer 2016	Northeast Mid-Atlantic	June 18–27	7
	Mid-West	Aug 01–14	10
	South Central	Aug 16–28	9
Winter 2017	South Central	Jan 30 – Feb 12	8
	Mid-West	Feb 13–26	9
	Northeast Mid-Atlantic	Feb 27 – Mar 10	9
Fall 2017	Northeast Mid-Atlantic	Oct 03–14	7
	Mid-West	Oct 16–27	8
	South Central	Oct 30 – Nov 10	7
Spring 2018	South Central	Apr 12–22	9
	Mid-West	Apr 23 – May 02	8
	Northeast Mid-Atlantic	May 04 – May 20	9

^a Transit flights between regions are attributed to their destination region

234 but substantial differences in bias between region and season (Chen, Zhang, Zhang, et
 235 al., 2019). ABL heights for CarbonTracker are obtained using NOAA’s Observation Pack-
 236 age (OBSPACK, Masarie et al., 2014) for CT2017 and CT-NRT-2019.2. We find that
 237 CT-NRT-2019.2, CT2019, and CT2017 have very similar ABL heights along ACT flight
 238 tracks.

239 CT2017 assimilates CO₂ observations from 254 sites to estimate a weekly set of biome-
 240 specific scaling factors for North America that are applied to prior biospheric [CO₂] flux
 241 model estimates. The scaling factors adjust the fluxes in order to minimize the differ-
 242 ence between modeled and observed atmospheric [CO₂]. These biome-specific scaling fac-
 243 tors are estimated independently for each of the 19 potential biomes within each TransCom
 244 regions (Gurney et al., 2002). Prior flux estimates for fossil fuel and wildfire CO₂ fluxes
 245 are not optimized. To estimate the impact of biases in prior fluxes, CT2017 uses two sets
 246 of priors (two each for terrestrial, ocean, fossil-fuel and wildfire carbon fluxes) and the
 247 final inversion result is the mean flux of the two inversions.

248 Two versions of the CASA model (Carnegie-Ames Stanford Approach Potter et al.,
249 1993, 2003) are used for the terrestrial biospheric prior and originate from the GFED
250 (Global Fire Emission Database) project (van der Werf et al., 2006; Giglio et al., 2009,
251 2013). Monthly net ecosystem carbon exchange from CASA as used in GFED 4.1s and
252 GFED_CMS are scaled to 3-hourly fluxes similar to Olsen and Randerson (2004), while
253 ensuring smooth month to month transitions following Rasmussen (1991). GFED 4.1 and
254 GFED_CMS are also used as priors for wild-fire fluxes and rely on MODIS (MODerate
255 resolution Imaging Spectrometer) fire counts and CASA to estimate wildfire carbon loss.

256 As prior for fossil fuel emissions the ODIAC2016 and *Miller* datasets are used in
257 CT2017. The *Miller* dataset uses estimated total global fossil fuel CO₂ emissions from
258 the Carbon Dioxide Information and Analysis Center (CDIAC, Boden et al., 2016), which
259 are spatially mapped to a 1°×1° grid using the spatial patterns of the EDGAR4.2 in-
260 ventory (Comission, 2019) and temporal distribution of Blasing et al. (2005). ODIAC
261 (Oda & Maksyutov, 2011) emissions are also based on CDIAC, but differs in the spa-
262 tial mapping of fluxes, which is based on proxy data such as power-plant locations, night-
263 light images, and aviation tracks. Because of ODIAC's yearly temporal resolution, sea-
264 sonal changes were derived using CDIAC monthly fossil fuel emission inventories (Andres
265 et al., 2011). Diurnal and day of the week fossil fuel cycles are imposed on monthly emis-
266 sions using scaling factors (Nassar et al., 2013).

267 For ocean basins, oceanic, instead of biospheric, CO₂ fluxes are optimized. Both
268 ocean priors – the Ocean Inversion Flux prior (OIF, Jacobson et al., 2007) and pCO₂-
269 Clim (Takahashi et al., 2009) – are based on estimates of air-water differences in CO₂
270 partial pressure from either ocean inversions (OIF) or direct observations (pCO₂-Clim).

271 Consequently, CT2017 provides a complete set of carbon surface fluxes from the
272 terrestrial biosphere, oceans, fossil fuels and wildfires as well as atmospheric CO₂ mole
273 fractions, which are available at 3-hourly temporal resolution and 1° × 1° spatial res-
274 olutions over North America. CO₂ mole fractions are reported on TM5's 25 model lay-
275 ers (Krol et al., 2005), which include 6 layers below 1.5 km and 15 layers below 10 km.
276 CarbonTracker has unrealistically large differences between the first (25 m) and second
277 (103 m) atmospheric layer in well-mixed conditions (Díaz-Isaac et al., 2014). However,
278 these model levels are considerably below the typical ABL level-leg flight altitude of ~
279 330 m AGL. CT2017 includes parameterized convective CO₂ mass-flux.

2.1.2 WRF-Chem

The mesoscale model is WRF-Chem v3.6.1 (Powers et al., 2017; Skamarock et al., 2008; Grell et al., 2005; Fast et al., 2006) with the modification to transport greenhouse gases as passive tracers described in Lauvaux, Schuh, Uliasz, et al. (2012). Trace gas boundary conditions are provided from CarbonTracker at 3-hourly interval posterior CO₂ mole fractions and surface fluxes introduced in the last subsection. An extra step is taken to assure the conservation of mass when ingesting CarbonTracker CO₂ mole fractions into the WRF-Chem domain. More details of the mass conservation of CO₂ can be found in Butler et al. (2020).

The domain of interest contains most of North America at 27 km horizontal resolution. The model has 50 levels up to 50 hPa with 20 levels in the lowest 1 km. The model meteorology is initialized every 5 days and driven with ERA5 reanalysis every 6 hours at 25 km horizontal resolution. The WRF-Chem dynamic is relaxed to ERA5 meteorology every 6 hours using grid nudging. Each meteorological re-initialization is started at a 12-hour setback from the end of the previous 5-day run. The first twelve hours of every 5-day simulation are considered spin-up and discarded from the final analysis. We also update sea surface temperature every 6 hours at 12-km resolution. Choices of the model physics parameterizations used in this experiment are documented as the baseline setup in Feng, Lauvaux, Davis, et al. (2019) and Feng, Lauvaux, Keller, et al. (2019) and model output for all ACT campaigns is archived and publicly available at the Pennsylvania State University DataCommons (Feng et al., 2020).

CO₂ fluxes in WRF are taken from CarbonTracker as described above and remain separate tracers in the model simulations. For analyses requiring total atmospheric CO₂ mole fractions, the surface flux tracers are summed and added to the boundary condition CO₂ tracer.

2.2 Analysis of CO₂ residuals

Differences between modeled and observed CO₂ are calculated by subtracting [CO₂] observed along the aircraft flight from modeled [CO₂] using the nearest neighbor in space and time. Chen, Zhang, Zhang, et al. (2019) found while comparing CT-NRT v2017 to ACT observations that temporal and spatial interpolation impacted calculated RMDSs of typically less than 0.4 ppm in the ABL, which is considerably smaller (order 10% or

311 less) than RMSDs calculated in this work. The resulting residuals thus include both er-
 312 rors from model transport and surface fluxes. Given that CT and WRF use the same
 313 flux dataset, differences in residual should be a representation of differences in atmospheric
 314 transport including model resolution.

315 We calculate statistical measures – including bias, median deviation, root mean square
 316 deviation, and mean absolute deviation – for the entire data set as well as separated by
 317 region, season, and meteorological airmass. Confidence intervals for the above statisti-
 318 cal measures are calculated using a block-bootstrap, which accounts for temporal auto-
 319 correlation using an *optimal block-length* approach (Politis & White, 2004; Patton et al.,
 320 2009). For each subset of the data, we also separate the dataset by vertical flight level.
 321 These divisions enable us to gain more understanding of the causes for model-data dif-
 322 ferences such as the impact of biological fluxes from different regions, and the impact of
 323 vertical mixing on continental background [CO₂].

324 We adopt the following notation for all quantities: The observed arithmetic mean
 325 and standard deviation of a quantity x are presented as $\bar{x} \pm \sigma$.

326 2.3 Variograms

327 To assess spatial statistics of CO₂ residuals, we compute empirical (semi-)variograms
 328 (Matheron, 1963) for each flight day:

$$\gamma(D) = \frac{1}{2|N(D)|} \sum_{N(D)} (R_i - R_j)^2, \quad (1)$$

329 where $N(D)$ is the set of all pairwise Euclidean distances ($i - j$), $|N(D)|$ the number
 330 of distinct pairs, and R_i and R_j are the residuals at spatial locations i and j . Distance
 331 (on WGS84 ellipsoid) pair calculation and is performed separately for individual level-
 332 legs at each altitude level, to minimize the impact of atmospheric change. Vertical dis-
 333 tances are not included in the variogram calculations as horizontal distances are much
 334 larger than altitude differences within the same level-leg. Subsequently, the empirical var-
 335 iograms for ABL, LFT, and HFT as well as WRF and CT are calculated using all dis-
 336 tance pairs. Euclidian distance calculations are performed using *Experimental (Semi-)*
 337 *Variogram* version 1.4.0 (Schwamhart, 2013). Distances are binned into 36 classes us-
 338 ing a geometric scaling between 1 and 750 km. To remove the disproportionate impact
 339 of outliers, including local CO₂ plumes (e.g. directly downwind of conventional power

plants) that caused spikes of more than 100 ppm in [CO₂], on variance calculations, we only considered [CO₂] residuals between the 1st and 99th percentiles for the variogram.

To characterize spatial residual statistics, we fit an exponential variogram of form

$$\gamma(D) = c_0 + c_1 \left(1 - \exp\left(\frac{-D}{L}\right) \right), \quad (2)$$

to the observational data, where c_0 is the nugget (y-intercept of variogram), c_1 the sill (the limit of γ at infinite D) and L the characteristic length-scale of the variogram. As proposed by Schwanghart (2013), the range (distance at which the γ approximates the sill is assumed to be $3L$. The exponential fit is conducted with Matlab2018b's *lsqnonlin*-solver using weighted least squares using the inverse of the standard deviation of CO₂ residuals in each distance bin and a lower parameter bound of 0 is enforced for nugget, range, and sill.

3 Results and discussion

This study considers a total of 402,838 [CO₂] observations collected during four ACT campaigns which are compared to modeled [CO₂] from CT and WRF (Figure 2 and Supporting Table S1). The models appear to be capable of reproducing the multimodal shape of observed [CO₂], which is both caused by the seasonality of CO₂ fluxes and mixing, and the general increase of mean atmospheric CO₂ between 2016 and 2018 associated with anthropogenic carbon emissions. The resulting [CO₂] residuals for CT and WRF follow near symmetric, peaked distributions with high kurtosis (~ 59 and ~ 42 for CT and WRF, respectively) and near zero mean (CT: -0.34 ± 3.12 ppm; WRF: 0.82 ± 4.37 ppm for mean \pm standard deviation). These residual distributions are clearly and significantly different (Figure 2c) from normal distributions with identical means and standard deviations. Skewness is small compared to kurtosis (-2.1 and 2.7 for CT and WRF) but of opposite sign indicating skew towards negative bias for CT and positive bias for WRF. Note that the mode of the residual histogram is slightly positive (<0.5 ppm) for both models.

The skewness of residuals can be attributed to CT's apparent lack of modeled [CO₂] in excess of approximately 416 ppm, while WRF underpredicts [CO₂] at values below approximately 400 ppm (Figure 2a+b). CT's more pronounced [CO₂] peak at approximately 412 ppm is attributed to the fact that CT exhibits a narrower range of modeled ABL [CO₂] during winter and spring compared to both ACT observations and WRF (Supporting

370 Figure S1). Consequently, CT’s winter and spring $[\text{CO}_2]$ in the ABL show much less over-
 371 lap with fall and summer $[\text{CO}_2]$ and the resulting PDF appears less smooth (Support-
 372 ing Figure S1 b) compared to the corresponding PDFs of ACT observations and WRF.
 373 Furthermore, the too narrow peak in CT can be attributed mainly to the Northeast Mid-
 374 Atlantic region (Supporting Figure S2).

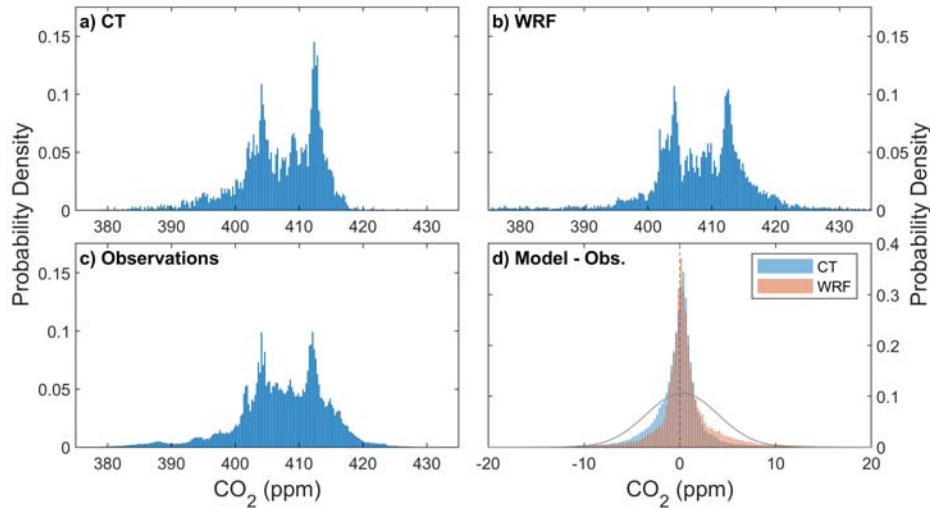


Figure 2. Overview of modeled and observed CO₂ mole fractions during four ACT campaigns 2016-2018. (a) CarbonTracker (CT); (b) WRF-Chem; (c) Aircraft observations; and (d) resulting CO₂ (Modeled – Observed CO₂) for CT and WRF. The grey line in (d) shows the normal distribution with similar mean and standard deviation to WRF residuals for reference.

375 3.1 Characterization of CO₂ residuals

376 For the remainder of the analysis, we focus on $[\text{CO}_2]$ residuals and their spatio-temporal
 377 statistics. This limits the impact of increasing ambient $[\text{CO}_2]$ due to fossil fuel emissions
 378 and seasonal CO₂ climatologies on our analysis. Division of residuals by altitude level
 379 (Figure 3) reveals that the total difference (Figure 2 d) in $[\text{CO}_2]$ residual distribution be-
 380 tween WRF and CT is primarily reflective of differences in the ABL. Here, CT exhibits
 381 a more peaked distribution with negative bias, while WRF’s distribution is wider and
 382 with positive bias. The overall shape of CT and WRF residual distribution is non-Gaussian
 383 at all levels for CT and WRF and becomes markedly narrower and more peaked with
 384 increasing height, while the ABL $[\text{CO}_2]$ exhibits pronounced *heavy tails*. Comparing the

385 residual distributions between CT and WRF (Figure 3, right column) shows that the dif-
 386 ference in residual PDFs in the ABL is not only due to the difference in mean residu-
 387 als between CT and WRF, but also due to the opposite skewness of the underlying resid-
 388 ual distributions. For free tropospheric levels (LFT, HFT), we find that that the differ-
 389 ence in residual PDFs is primarily caused by a shift in the mean of the distribution (i.e.
 390 bias) rather than the shape of the distribution.

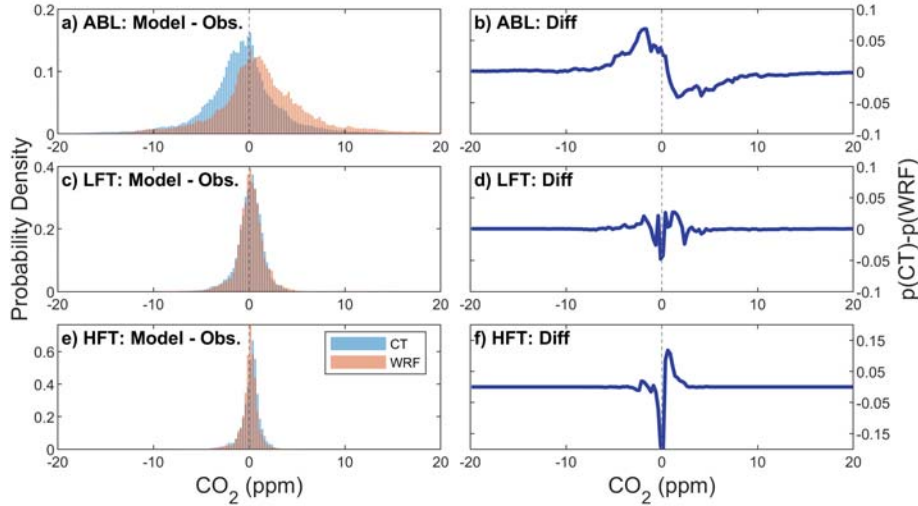


Figure 3. Probability density of model observation CO_2 residuals for CarbonTracker and WRF-Chem separated by vertical level: (a) atmospheric boundary-layer – ABL; (c) lower free troposphere – LFT; (e) higher free troposphere – HFT; and differences in their respective probability density functions (b,d,f).

391 Figure 3 a also reveals that while the majority of ABL $[\text{CO}_2]$ residuals fall into a
 392 narrow range (Interquartile range of -2.76–1.07 ppm and -1.07–3.87 ppm, respectively;
 393 Supporting Table S1) compared to the entire range of residuals, residuals are heavy tailed.
 394 To characterize this larger range of residuals, we also calculated the 2.5th and 97.5th per-
 395 centiles, which presents a compromise between representing the tail ends of the resid-
 396 ual of the distribution, while not including outliers, which for example can result from
 397 CO_2 plumes in the vicinity of power plants.

398 We find that the general picture encountered for the residual PDFs (Figure 3, left
 399 column) holds generally true when residuals are separated by season, region, and airmass

400 (Figure 4 and Supporting Table S1). While we encounter that mean residual and IQR
401 vary across cases (see discussion in the following section), ABL IQRs are within the range
402 of ± 5 ppm (see also Supporting Table S1). At the same time, the tails of the residual
403 distribution are much larger in magnitude for both CT and WRF and can exceed -10 ppm
404 and 15 ppm for the 2.5th and 97.5th percentiles, respectively. At the higher LFT and HFT
405 levels, the range of the residual PDF is much smaller and typically with ± 5 ppm (LFT)
406 and ± 2.5 ppm (HFT).

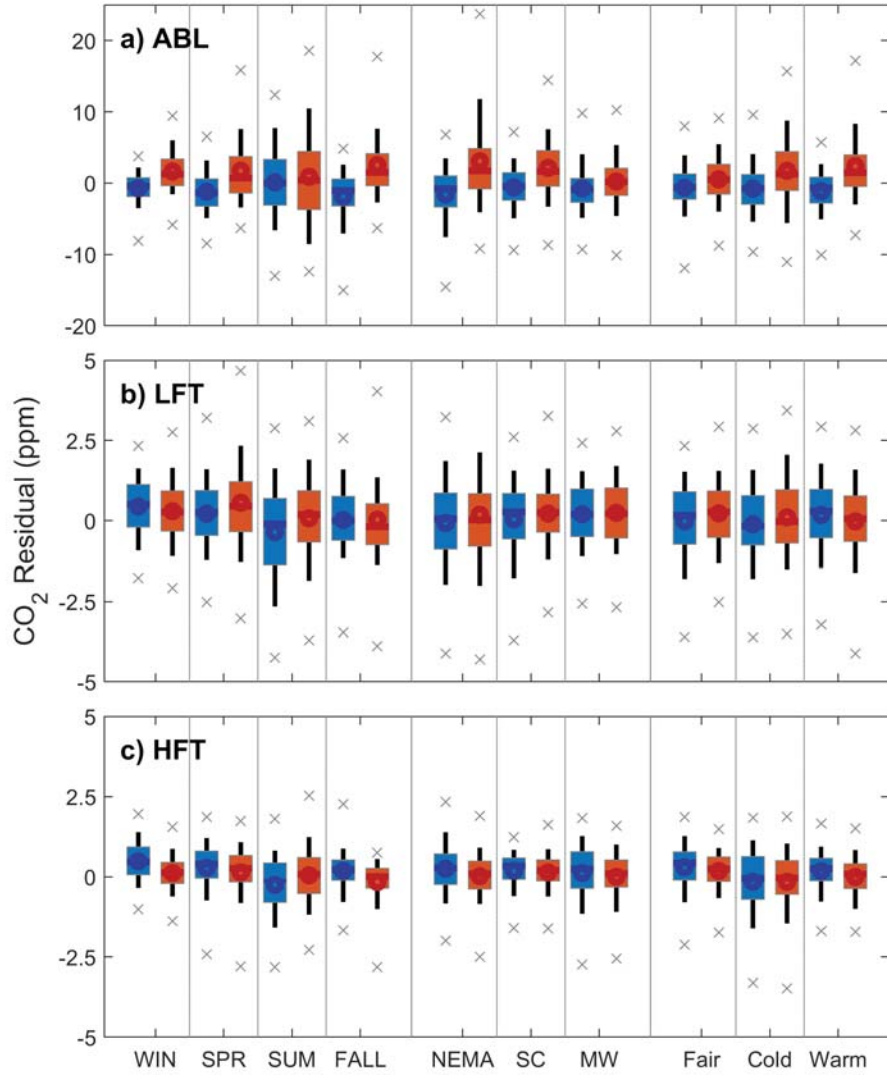


Figure 4. Box and whisker of $[\text{CO}_2]$ residual distributions from CT (blue) and WRF (red) for seasons, regions, and airmasses in (a) atmospheric boundary-layer – ABL; (b) lower free troposphere – LFT; (c) higher free troposphere – HFT. The median and mean are indicated by horizontal lines and circles, respectively. The box indicates 25th and 75th percentiles, whiskers 10th and 90th percentiles, and grey crosses indicate the 2.5th and 97.5th percentiles.

407 A quantile by quantile (Q-Q) comparison of CT and WRF residuals to normal dis-
408 tributions with corresponding means and standard deviations (Supporting Figure S3)
409 further reinforces the notion of non-Gaussian [CO₂] residuals encountered for the entire
410 dataset holding true across seasons, regions, and airmasses. The Q-Q plots also reveal
411 the largest deviations from Gaussian behavior for CT and WRF to be at the tail ends
412 of the residual PDFs, further highlighting the potential of large magnitude residuals to
413 impact summary statistics such as bias or RMSD, which are commonly used to constrain
414 inversion systems.

415 *3.1.1 Regional, seasonal, and airmass dependent bias and RMSD*

416 Past studies of model observation mismatch have often reported on bias and root
417 mean square deviation (RMSD) between model and observations (Figure 5). The me-
418 dian residual and Mean Absolute Deviation (MAD) are reported in Supporting Figure S4.
419 As expected, biases for LFT and HFT are much closer to zero compared to biases in the
420 ABL. There are substantial disagreements between CT and WRF both in magnitude and
421 sign of the bias. For higher atmospheric levels for which effects of local fluxes and mix-
422 ing are less important – and thus are more likely to reflect background conditions – CT
423 and WRF show closer agreement.

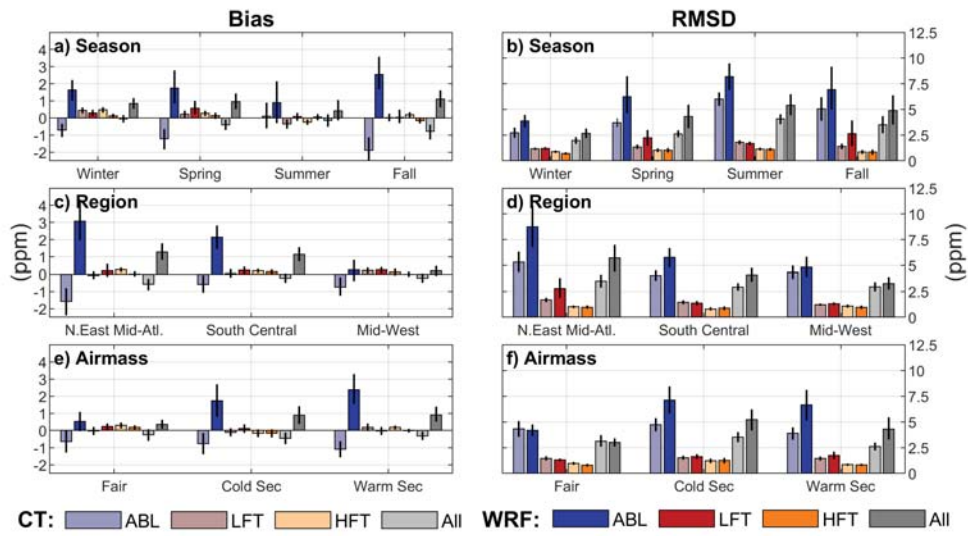


Figure 5. Comparison of CarbonTracker and WRF-Chem bias (a,c,e) and RMSD (b,d,f) for levels ABL, LFT, and HFT and separated by climatological season (a,b), region (c,d), and air-mass (e,f). Bootstrapped 95% confidence intervals, using a block bootstrap (see methods) are shown in black.

424 With respect to climatological seasons (Figure 5 a), WRF and CT show similar be-
 425 havior in the total magnitude of biases in the ABL, but signs are opposite between CT
 426 and WRF, while LFT and HFT biases are comparatively small (typically $< |0.5|$ ppm).
 427 Fall and Spring show the worst model performance for both CT (-1.89 ± 4.70 ppm; -1.22 ± 3.50 ppm,
 428 respectively) and WRF (2.53 ± 6.46 ppm; 1.75 ± 5.99 ppm, respectively), followed by Win-
 429 ter and Summer. For Summer, CT has a near-zero bias (0.10 ± 6.01 ppm), while the bias
 430 from WRF remains considerable (0.89 ± 8.13 ppm). Interestingly, the comparatively large
 431 bias for Fall is confined to the ABL, while LFT and HFT biases are virtually absent. This
 432 is in contrast to Winter, when model observation mismatch in the ABL also extend to
 433 positive biases at LFT and HFT levels.

434 Seasonal Root Mean Square Deviation (RMSD, Figure 5 b) for CT and WRF in-
 435 crease from Winter to Summer and then decrease slightly during Fall, which is consis-
 436 tent with the frequency of occurrence for cloud convection.

437 Overall, the median difference (Supporting Figure S4) is much smaller than the bias
 438 for ABL, indicating that the heavy tails of the residual distribution contribute consid-
 439 erably to the overall bias. For LFT and HFT, median residual and bias are similar to
 440 each other.

441 Comparing CT and WRF residuals by study region (Figure 5 c), we find that both
 442 CT and WRF struggle in particular to accurately represent ABL $[\text{CO}_2]$ (biases in ex-
 443 cess of ± 1 ppm) in the North East Mid-Atlantic region, which has the most complex ter-
 444 rain of the three study regions and also exhibits complex atmospheric flow patterns. In
 445 contrast, Mid-West and South Central regions exhibit comparable biases for CT of -0.74 ± 4.26 ppm
 446 and -0.60 ± 3.99 ppm, while WRF has a high bias of 2.14 ± 5.37 ppm in the South cen-
 447 tral and a near zero bias (0.23 ± 4.82 ppm) in the Mid-West ABL. Different from seasonal
 448 RMSD patterns, regional RMSD is comparable in magnitude between CT and WRF,
 449 except for NEMA where RMSDs in ABL and LFT are $\sim 60\%$ larger for WRF compared
 450 to CT. Generally speaking median residuals exhibit a similar behavior, but with a smaller
 451 magnitude (< 1.5 ppm for all cases).

3.1.2 Comparison to previous studies

[CO₂] uncertainties over North America have been addressed in previous studies either through comparison of models with concentration tower observations or through model-model comparison.

A previous effort to characterize uncertainties stemming from biospheric carbon fluxes and atmospheric transport using perturbed WRF-Chem ensembles over North America during summer 2016 (Chen, Zhang, Lauvaux, et al., 2019) found that near surface [CO₂] uncertainties arising from fluxes (~ 6 ppm) exceed transport uncertainty (~ 4 ppm) during the daytime, while background uncertainty was less important (~ 1 ppm). In the free troposphere, the importance of flux and transport uncertainty were both reduced to ~ 1 ppm respectively (with transport uncertainty exceeding flux uncertainty), while background uncertainty remained unchanged. These uncertainties are comparable in magnitude to standard deviations of summertime model observation residuals for WRF found in this study (ABL: 8.13 ppm, LFT: 1.67 ppm; Table S1).

Chen, Zhang, Lauvaux, et al. (2019) identified the Mid-West and Mid-Atlantic as regions of largest model uncertainty due to terrestrial carbon fluxes, and noted that strong horizontal and vertical CO₂ gradients in this region also give rise to larger uncertainties due to transport. Results from our study also show large [CO₂] residuals in the NEMA region, but smaller errors in the Midwest, albeit for all seasons taken together.

Our result that model observation mismatches were largest in NEMA is supported by Chen, Zhang, Zhang, et al. (2019), who compared ACT to CT-NRT v2017 and CAMS for Summer 2016 and Winter 2017 and found negative biases for CT-NRT in the Mid-Atlantic for Summer 2016. CT-NRT's Summer 2016 ABL bias averaged across all regions was approximately -1.5 ppm while CT data used in this study had near zero bias and WRF had a positive bias of ~ 1 ppm. A comparison to CAMS (Copernicus Atmosphere Monitoring Service) showed that CAMS biases were much larger in magnitude compared to the biases found in this work. Chen, Zhang, Zhang, et al. (2019) also identified the NEMA as a region of high bias and particularly during Summer. Given the fact that NEMA is downwind of MW, which is the region of largest uncertainty in terrestrial carbon fluxes (Chen, Zhang, Lauvaux, et al., 2019; Feng, Lauvaux, Davis, et al., 2019), model data mismatches in this region are likely to result from both flux and transport uncertainty. RMSDs in this work are also comparable in magnitude to RMSDs cal-

484 culated using a WRF-model ensemble of approximately 4.5 ppm for daily values and 4 ppm
485 for 7–10 day averaging (Feng, Lauvaux, Keller, et al., 2019), who also identified the bio-
486 sphere as the major source of ABL model uncertainty (~ 3 ppm). This uncertainty was
487 invariant to averaging at less than seasonal timescales, while transport uncertainty di-
488 minished when averaged over time (~ 2 ppm and 1 ppm for averaging windows of 1 and
489 10 days), becoming less important than uncertainties from boundary inflow and fossil
490 fuels. Given that ACT’s insitu $[\text{CO}_2]$ observations reflect air mass history, flux error is
491 likely a large portion of RMSDs encountered in this work.

492 A tower-based comparison of WRF-Chem and Carbontracker/TM5 using CT2009
493 fluxes during the growing season of 2006 (Díaz-Isaac et al., 2014) highlighted the impacts
494 of modeled near surface dynamics on ABL $[\text{CO}_2]$. While CarbonTracker underestimated
495 CO_2 drawdown during summer, WRF had a tendency to overestimate drawdown, while
496 using the same set of surface fluxes. Additionally, the authors found that WRF exhib-
497 ited shallower ABLs with small within-ABL vertical gradients, indicating more well mixed
498 conditions in the ABL compared to TM5/Carbontracker, whereas TM5 /Carbontracker
499 showed stronger vertical mixing between ABL and free troposphere. Our results (Fig-
500 ure 5) show a tendency in CT to have opposite biases between ABL and LFT, which may
501 be indicative of excess vertical mixing in CT. WRF, in contrast, has a more consistent
502 positive bias at all levels.

503 Model resolution is also an important factor for model performance. A compari-
504 son of $[\text{CO}_2]$ surface observations to the CAMS CO_2 forecasting system showed a 1.8-
505 2.5 ppm reduction of RMSD (corresponding to 33%), when reducing horizontal model
506 resolution from 80 km to 9 km (Agustí-Panareda et al., 2019). This was attributed to both
507 better representation of modeled wind fields (i.e. transport) and spatial variability in sur-
508 face carbon fluxes. While the WRF-Chem resolutions used in this studies had a 27 km
509 resolution and surface fluxes were at $1^\circ \times 1^\circ$ resolution, RMSDs of order 5 ppm encoun-
510 tered for ACT were comparable to CAMS RMSDs at 9 km. At the same time, WRF RMSDs
511 were larger than those of CT at the coarser 1-degree resolution, conflicting with results
512 found by Agustí-Panareda et al. (2019). One potential explanation for this discrepancy
513 is the fact that while neither WRF nor CT are capable of directly resolving convective
514 cells, WRF has a sufficiently high resolution to resolve features of warm and cold fronts.
515 Consequently, small errors in frontal location and other synoptic features can lead to large
516 errors in modeled $[\text{CO}_2]$ in WRF, while CT does not have the same small-scale variabil-

ity and thus shows lower total bias but a less realistic distribution of $[\text{CO}_2]$ (Figures 1 a–
 c and Supporting Figures S1-S2). This hypothesis is consistent with the fact that Sum-
 mer, which has the most active cloud convection, shows small bias in WRF but the largest
 RMSD (Figure 5). Additionally, posterior carbon fluxes have been optimized for CT and
 not for WRF. The differing behavior between CT and WRF and the effect of flux op-
 timization are further discussed in section 3.2. It remains to be seen whether a further
 reduction of WRF resolution below 27 km, which would allow for convection resolving
 simulations, would increase model accuracy or would further exacerbate errors due to
 location errors of synoptic structures, which do not appear in the coarser CT.

The CarbonTracker inversion system (Peters et al., 2007) uses RMSD between ob-
 servations and atmospheric model to estimate its assumptions for model-data mismatch
 (MDM) that constrain the inversion system (specifically: $\text{MDM} = 0.85\text{-}0.95 \times \text{RMSD}$).
 CT’s choice of using seasonally, regionally, and vertical level specific MDM values ap-
 pears to be justified, based on our results, that residuals strong vary between region, sea-
 son, and level (Figures 3–5). At the same time, other inversion systems such as CarbonTracker-
 Lagrange (CT-L, Hu et al., 2019) do not specify seasonally differing MDMs. Given CT-
 L’s regional focus and finer resolution, seasonally varying MDMs appear to be advan-
 tageous given our findings of seasonally varying model residuals.

Note that the previous studies discussed here did not perform a weather aware anal-
 ysis in the sense that they did not separate model observation comparisons by airmass
 or weather conditions. In fact, when comparing aircraft observations to models, there
 are likely issues of representativeness, as for example NOAA/GML Global Greenhouse
 Gas Reference Network profiles (Sweeney et al., 2015) are collected using small aircraft,
 which are limited to operating in fair weather conditions.

3.1.3 Interpretation of large residuals

Given the importance of characterizing model-observation-mismatch for atmospheric
 inversion results and given the fact that our model residual statistics are heavily influ-
 enced by the long tails of the $[\text{CO}_2]$ residual PDF, we proceed to investigate what con-
 ditions are most conducive to the occurrence of large magnitude residuals. To do so, we
 chose to focus on the ABL $[\text{CO}_2]$ residuals in the tails ($< 5^{th}$ and $> 95^{th}$ percentiles)
 of the distribution. We also chose to concentrate on WRF, which due to its higher res-

548 olution is more capable of resolving frontal structures. We find that large magnitude resid-
549 uals were not randomly distributed across all flight days, but rather concentrated on spe-
550 cific days for which model observation residuals tended to be large. For example, the 10
551 days with the largest fraction of large positive $[\text{CO}_2]$ residuals contributed to 72% of all
552 positive large magnitude residuals. Additionally, 9 out of 10 days were associated with
553 research flights that included a frontal crossing and 6 out of 10 days were for the NEMA
554 region. At the negative residual tail end, we found that 10 days contributed to 68% of
555 all large magnitude residuals. These days with large negative residuals were highly con-
556 centrated during Summer (8 out of 10) and specifically the MW region (5 days during
557 Summer). Unlike the positive residual days, weather did not appear to play a major role
558 during negative residual days, which may be due to the fact carbon fluxes in MW are
559 underestimated for the MW agricultural belt, such that transport errors associated with
560 synoptic systems do not play a considerable role.

561 The fact that large magnitude positive residuals are concentrated during frontal
562 conditions, highlights the fact that CO_2 transport and associated model errors are highly
563 dependent on synoptic scale conditions. It is likely that comparatively small errors in
564 modeled frontal location, which arise despite WRF being nudged to ERA-5 analysis, com-
565 bined with observed large cross frontal $[\text{CO}_2]$ differences (Pal et al., 2020) can result in
566 large $[\text{CO}_2]$ residuals. Also, ACT observations revealed characteristic bands of elevated
567 $[\text{CO}_2]$ ahead of the cold front, which the WRF model may not be able to adequately re-
568 produce. Given the importance of synoptic weather systems to mid-latitude carbon trans-
569 port (e.g. Parazoo et al., 2008, 2011) as well as the large associated model residuals, weather
570 aware specification of prior model observation mismatch could be beneficial for inver-
571 sion systems and particularly regional inversions. The interplay between season and air-
572 mass on model residuals is further discussed in section 3.2.

573 The large contribution of MW summer to negative residuals (i.e. overestimation
574 of modeled $[\text{CO}_2]$ within the ABL) coincides with the fact that the U.S. Midwest is dom-
575 inated by high intensity agriculture and particularly corn, which makes this region a large
576 continental carbon sink during the agricultural growing season, leading to CO_2 deple-
577 tion within the ABL. Consequently, underestimation of terrestrial carbon fluxes is a likely
578 source of this model data mismatch for this region. At the same time, tall ABLs dur-
579 ing summer and associated entrainment of free-tropospheric air counteract CO_2 in the
580 ABL, but models such as WRF can have considerable random errors in ABL heights that

581 are variable between regions (e.g. Díaz-Isaac et al., 2018). The covariance between ter-
 582 restrial carbon fluxes and ABL heights (also referred to as rectifier effect, Denning et al.,
 583 1995) makes it difficult to attribute model observation differences into flux and model
 584 errors. The impact of ABL heights and specifically differences in simulated ABL mix-
 585 ing between models (e.g. Díaz-Isaac et al., 2014) on $[\text{CO}_2]$ residuals is further discussed
 586 in section 3.2.3

587 *3.1.4 Implications for inversion systems*

588 The $[\text{CO}_2]$ model-observation residuals encountered in this study do not follow Gaus-
 589 sian distributions (Figures 2 + 3). Given that this study cannot separate between trans-
 590 port and flux errors, it is theoretically possible that the total residuals, which are non-
 591 Gaussian, are the result of normally distributed flux and transport errors which are su-
 592 perimposed onto each other. At the same time, we encounter non-Gaussian residuals at
 593 all vertical levels, including LFT and HFT, where the influence of surface fluxes is smaller
 594 compared to the surface, implying that transport model errors, taken in isolation, are
 595 also non-Gaussian. Atmospheric inversion systems require the specification of model-data
 596 mismatch errors in order to constrain the flux optimization. The CarbonTracker (Peters
 597 et al., 2007) and most other operational inversions require mismatches to be normally
 598 distributed and transport errors to be unbiased. While we find that the overall bias of
 599 the model-data mismatch is comparatively small, its non-Gaussian nature found in this
 600 study has the potential to impact inversion results. The heavy tails of the $[\text{CO}_2]$ resid-
 601 ual contribution, have outsized impacts on RMSD and standard deviation. The result-
 602 ing larger RMSDs and standard deviations, which are used to prescribe Gaussian errors,
 603 in consequence, reduce the sensitivity of inversion systems to observations. Given that
 604 we find that a large fraction of large magnitude model observation mismatches stem from
 605 a small number of days, and (in the case of positive residuals) from days with frontal ac-
 606 tivity, it appears that specifying weather aware model data mismatches in regional in-
 607 version systems could increase the sensitivity of the inversion to observations and thus
 608 improve flux estimates.

609 **3.2 Comparison of model residuals between CT and WRF**

610 A comparison of the joint residual statistics (Figure 6) reveals their differing be-
 611 havior in the two modeling systems when disaggregated according to seasons, regions,

612 and airmasses. Given that CT and WRF use identical carbon surface fluxes and that
613 WRF uses $[\text{CO}_2]$ from CT as lateral boundary condition, we infer that differences be-
614 tween CT and WRF are due to tracer transport differences.

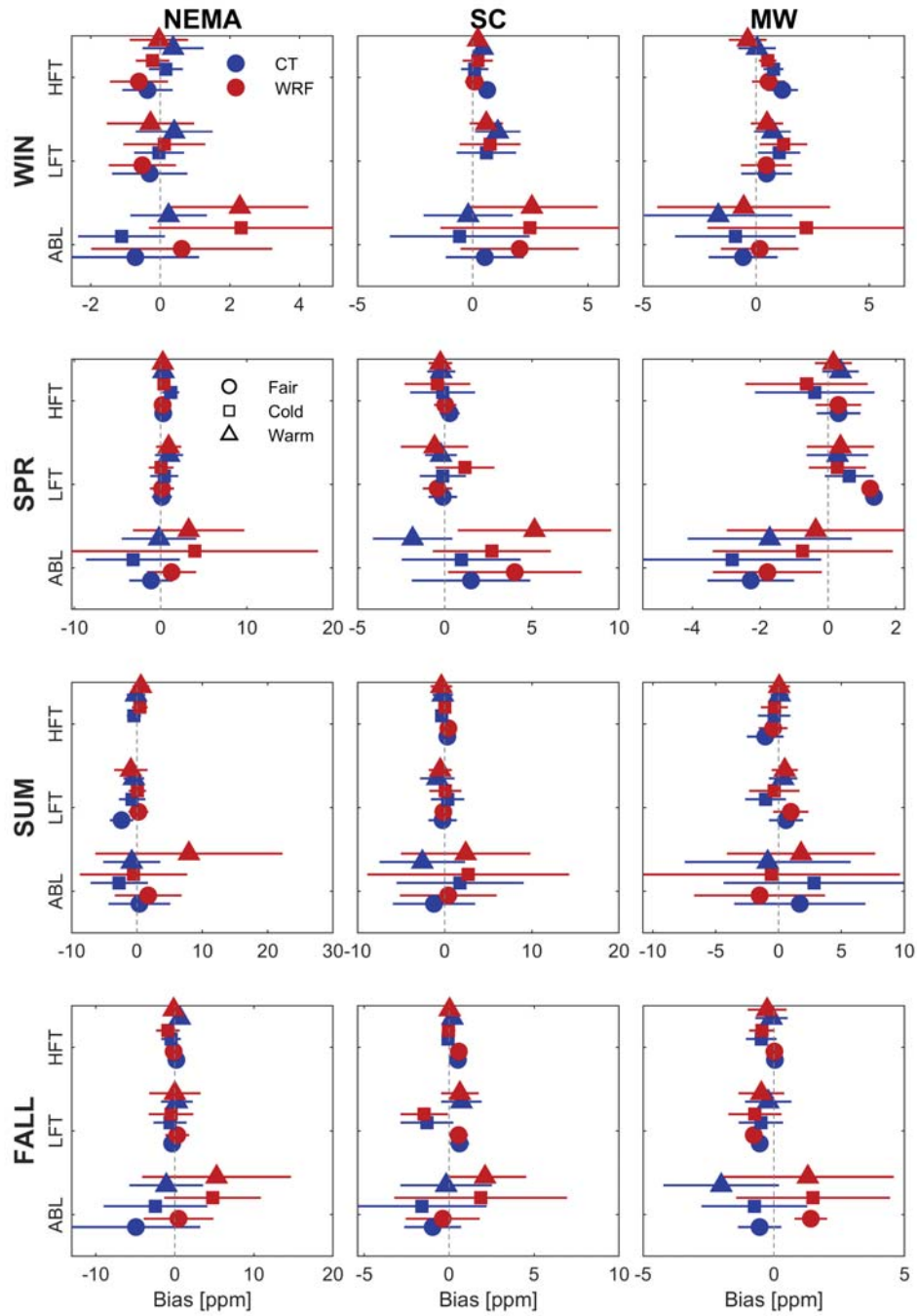


Figure 6. Comparison of CarbonTracker (as described in methods) and WRF-Chem CO₂ residual as function of climatological season (rows), region (columns) and airmass (symbols) for the three observation levels.

3.2.1 Residuals in the free troposphere

Free tropospheric $[\text{CO}_2]$ residuals are small compared to ABL residuals for all seasons (Figures 6 and Supporting Figure S5 showing only FT and HFT), regions, and air-mass conditions and mean differences between CT and WRF are smaller than their respective standard deviations. The magnitude of HFT bias is of order 0.5 ppm for both CT and WRF, while the standard deviation of residuals is of order 1 ppm. In the vast majority of cases CT and WRF bias differences are less than 0.5 ppm and show the same sign. A similar picture emerges for LFT, but with slightly larger magnitude biases and standard deviations (|0.8| ppm and 1.5–2 ppm, for mean and standard deviation, respectively). Similarly, the difference between CT and WRF also tends to be less than 0.5 ppm and to be of similar sign (Supporting Figures S6–S12). The fact that model-model mismatches are of similar magnitude to model observation mismatch, highlights the difficulties in separating the two. It is notable that WRF tends to have lower free tropospheric $[\text{CO}_2]$ than CT, except during Summer where the reverse appears to be true for NEMA and MW, but not necessarily SC, where onshore flow of homogeneous high CO_2 air from the Gulf of Mexico occurs. Given the fact that CT and WRF employ the same carbon fluxes and WRF uses CT atmospheric mole fraction for lateral boundary conditions (i.e. background), it appears reasonable to infer that transport uncertainty between CT and WRF in the free troposphere is of order 0.5 ppm. However, given the comparatively large volume of the free troposphere compared to the atmospheric boundary-layer, even small model errors represent large quantities of carbon and will affect column averaged $[\text{CO}_2]$ (often referred to as XCO_2), which is thought to be less sensitive to ABL dynamics and surface flux heterogeneity (e.g. Keppel-Aleks et al., 2011). Also, it has been estimated that a difference of 0.5 ppm between to boundary-condition products over North America produces an offset of 0.8 PgC y^{-1} in the North American terrestrial carbon flux, which is similar to the magnitude to the actual North American sink of around $0.5\text{--}1.0 \text{ PgC y}^{-1}$ (Gourdji et al., 2012). This further highlights the need to further reduce uncertainties in global products. Additionally, given that the free troposphere is not in direct exchange with the surface, free tropospheric $[\text{CO}_2]$ biases can be integrated over continental scales, making attribution of flux errors to specific regions and processes difficult.

3.2.2 Interpretation of free tropospheric differences

CarbonTracker XCO₂ (CT2015) was also shown to have good agreement with aircraft observations using the NOAA aircore network with spatial XCO₂ gradients mostly reflecting large-scale circulation (Lan et al., 2017). Therefore, comparatively small free tropospheric biases are in line with our expectations. Sweeney et al. (2015) showed that vertically homogeneous oceanic background air becomes increasingly less homogeneous with residence time over land, in response to terrestrial carbon fluxes and upward mixing of the flux signal. Since, WRF and CT employ identical fluxes, differences between CT and WRF are either due to differences in vertical mixing or air mass history. Due to the fact that ABL volume and mass are small compared to the free troposphere, vertical mixing differences are difficult to diagnose using ACT data. However, since HFT and LFT [CO₂] are lower in WRF during winter, when the terrestrial biosphere acts as a carbon source and higher during summer, when there is carbon uptake, as well as the fact the CT has been documented to have strong vertical mixing (Díaz-Isaac et al., 2014; Schuh et al., 2019), the differences between WRF and CT with respect to ABL to FT [CO₂] are consistent with different vertical mixing strengths between models. These findings are also consistent with Butler et al. (2020), who found model data mismatches to result from model transport differences below 850 hPa. Cloud convection associated with frontal lifting causes convective mass flux and presents a potentially important avenue for vertical transport of CO₂. While CarbonTracker and the underlying TM5 chemical transport model operate on an approximately 4-times coarser horizontal resolution than WRF, CarbonTracker includes parameterized convective mass fluxes taken from the parent ECMWF (European Centre for Medium-Range Weather Forecasts) model. WRF in contrast, with its finer horizontal and vertical resolution, resolves a larger portion of vertical motion, but does not presently have explicitly coupled convective tracer mass-flux associated with clouds. This omission may cause underestimation of vertical transport, which is consistent with the observed opposite sign of ABL to FT CO₂ residuals between CarbonTracker and WRF found predominantly during Winter and Spring.

3.2.3 Residuals in the atmospheric boundary layer

A different picture emerges for ABL [CO₂] residuals (Figure 6). We encounter larger differences between CT and WRF. In the ABL, CT exhibits a low bias and WRF a high bias (Figure 3 a) for most seasons and regions. Exceptions include Summer in MW, for

677 which CT has high bias in cold and fair conditions, while WRF shows the opposite be-
678 havior. The differences in mean residual between models are generally smaller than one
679 standard deviation, highlighting the large temporal and spatial variability of model ob-
680 servation residuals. In general, we find the largest variation in $[\text{CO}_2]$ residuals as indi-
681 cated by their standard deviation during Summer conditions, which have the most ac-
682 tive cloud convection and biosphere fluxes. Winter, Spring, and Fall exhibit much less
683 variation, except for the NEMA region. In NEMA the standard deviations of residuals
684 remain large during Spring and Fall, which may be due to topographic effects, long con-
685 tinental upwind trajectories, and regional fossil fuel emissions. Fair weather conditions
686 on average are not only associated with the lowest magnitude in bias, but also show the
687 smallest differences between CT and WRF across seasons and regions.

688 This work investigates total ABL $[\text{CO}_2]$ biases as the difference between modeled
689 and observed $[\text{CO}_2]$ which consist of flux errors and transport uncertainty. Despite pre-
690 scribed carbon fluxes being optimized to continental $[\text{CO}_2]$ observations, ABL $[\text{CO}_2]$ bias
691 magnitudes for specific regions and seasons are approximately 1–3 ppm in Winter, 1–
692 10 ppm during Summer and 1–5 ppm during Spring and Fall, highlighting the remain-
693 ing uncertainties associated with biospheric carbon fluxes and atmospheric transport.

694 Because we use posterior carbon fluxes from CT, one can expect CT to show smaller
695 magnitude biases compared to WRF which has a different atmospheric transport of CO_2
696 – care should be taken to not interpret bias differences between WRF and CT as differ-
697 ences in model quality. Instead, model-model differences between CT and WRF should
698 be seen to reflect transport uncertainty. Model-model differences follow a similar sea-
699 sonal pattern compared to bias but can reach slightly larger magnitudes (Winter: 1–4 ppm;
700 Spring: 1–8 ppm; Summer: 1–10 ppm; Fall 1–8 ppm). We find larger model-model dif-
701 ferences for warm and cold airmasses associated with synoptic systems compared to fair
702 weather conditions. Also, biases are generally smaller in magnitude for fair weather, high-
703 lighting the role of dynamics processes on model performance. Model-model differences
704 encountered in our work are larger in magnitude compared to values found by Chen, Zhang,
705 Lauvaux, et al. (2019). A recent study using 45 different combinations of physical pa-
706 rameterizations in WRF (Díaz-Isaac et al., 2018) revealed ABL CO_2 transport uncer-
707 tainties of 3–4 ppm. Since model-observation differences are in the same range as model-
708 model differences, we can infer that transport uncertainty is a large contributor total ABL
709 $[\text{CO}_2]$ biases and must be resolved before reaching conclusions about flux errors alone.

710 In addition to substantial vertical $[\text{CO}_2]$ gradients resulting from ABL enrichment or de-
711pletion of $[\text{CO}_2]$ due to surface fluxes Pal et al. (2020) encountered large horizontal cross
712frontal $[\text{CO}_2]$ differences during Summer 2016, which arise from differences in airmass
713history as well as modification of surface fluxes in response to cloud shading and reduced
714ABL mixing (e.g. Chan et al., 2004; Pal et al., 2020). Given the importance of cross frontal
715 CO_2 differences for atmospheric CO_2 transport and potentially inversion system perfor-
716mance, it is important for atmospheric models to accurately represent these cross-frontal
717 $[\text{CO}_2]$ differences. Especially during Summer, when differences are largest with 5-30 ppm
718(Pal et al., 2020), we find differences in warm and cold sector bias in both models to ex-
719ceed 5 ppm, such that modeled cross-frontal $[\text{CO}_2]$ differences can differ considerably from
720observations. Smaller bias differences are found for the other seasons and regions, ex-
721cept for Winter in MW. However, given that Summer is a season with high convective
722activity and large terrestrial biogenic carbon fluxes, misrepresentation of cross-frontal
723gradients may have substantial impact on modeled atmospheric carbon fluxes and thus
724atmospheric inversions. This finding further highlights the potential need for weather-
725aware inversion approaches.

726 *3.2.4 Potential sources of mismatch*

727 The ABL is in direct contact with both the surface and the free troposphere, thus
728making accurate prediction of ABL $[\text{CO}_2]$ a particularly challenging problem. Despite
729using posterior biospheric CO_2 fluxes from CT, considerable uncertainty in surface car-
730bon fluxes remains an issue. Additionally, CT is optimized to continental scale CO_2 ob-
731servations and large variation of bias exists between regions, seasons, and airmass con-
732ditions. Besides surface fluxes, ABL growth and resulting entrainment of free tropospheric
733air into the ABL as well as convection lead to CO_2 exchange between ABL and LFT.
734Given the importance of vertical mixing for inversion accuracy (Stephens et al., 2007;
735Peylin et al., 2013; Schuh et al., 2019) we proceed to investigate potential impacts of ABL
736depth (in conjunction with ABL to LFT $[\text{CO}_2]$ differences) on model-model bias differ-
737ences. We find that CT tends to exhibit deeper ABLs for all seasons except Fall (Fig-
738ure 7), which would be consistent with, CT's demonstrated low bias for Winter and Spring
739(when ABLs are enriched in CO_2 compared to LFT) as well as the high bias during Sum-
740mer (when ABLs are depleted in CO_2). However, a more complicated picture emerges,
741when taking into account observed vertical $[\text{CO}_2]$ differences (Supporting Figure S13).

742 One caveat is the fact that this comparison uses ABL depths directly provided from CT
743 and WRF model output. For CT this means that ABL depths are calculated based on
744 the Richardson number, while WRF ABL depths are diagnosed in the turbulence pa-
745 rameterization. However, despite these differences in ABL definition, we believe that us-
746 ing the ABL definition native to the modeling system should accurately reflect the model's
747 vertical ABL mixing. Based on ABL depth differences between CT and WRF ranging
748 from -20% to 35% and typical ABL to LFT [CO₂] differences of less than 10 ppm mag-
749 nitude, we estimate the maximum impact of ABL depth differences between CT and WRF
750 to be less than 3 ppm. Consequently, while ABL [CO₂] bias differences between CT and
751 WRF during Winter are explainable by differences in entrainment of free tropospheric
752 air at the ABL-top, model-model residual differences between CT and WRF within the
753 ABL are considerably larger than 3 ppm for all seasons except Winter and can thus not
754 be explained by entrainment alone. This result leaves cloud convection associated with
755 frontal lifting and horizontal advection differences as the likely main source for the dif-
756 fering behavior between CT and WRF.

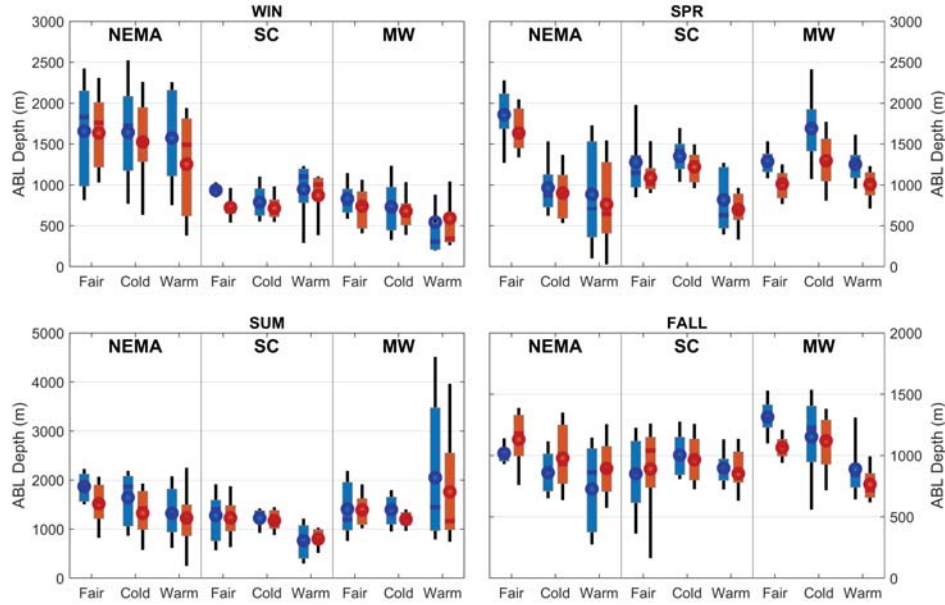


Figure 7. Comparison of CarbonTracker (as described in methods, red) and WRF-Chem (blue) diagnosed ABL heights separated by season, region, and airmass. The boxplot indicates 10th, 25th, 75th, and 90th percentiles of the distribution. The median and mean are indicated by horizontal lines and circles, respectively.

757 Differing $[\text{CO}_2]$ residuals between CT and WRF highlight the importance of CO_2
 758 transport differences in frontal systems. At the same time, considerable biases remain
 759 for CT and WRF shows larger magnitude biases than CT. We hypothesize that WRF,
 760 due to its higher resolution, is capable of reproducing frontal location and structure, while
 761 TM5 which underlies CT is less capable of doing so. CT's fluxes are optimized without
 762 taking into account transport uncertainty differences associated with frontal systems and
 763 using a model resolution that does not fully resolve synoptic scale weather. Consequently,
 764 terrestrial carbon fluxes optimized with the CarbonTracker system and applied to WRF,
 765 then lead to considerably higher $[\text{CO}_2]$ biases in warm airmasses compared to cold air-
 766 masses in WRF, while biases in warm and cold sectors for CT, which has a coarser res-
 767 olution, are more consistent.

768 Given the importance of midlatitude synoptic scale systems to North American merid-
 769 ional carbon transport, our findings support the notion that inversion systems can be

770 improved by considering the effects of frontal passage through, for example, warm and
771 cold sector specific prescribed model-data mismatches. At the same time, increasing pre-
772 scribed model-data mismatches near fronts without addressing model biases would de-
773 emphasize observations near frontal structures in inversion systems. This would poten-
774 tially reduce changes to prior fluxes in vicinity of synoptic systems, which may be es-
775 pecially problematic, because frontal systems present a complex environment, where sur-
776 face flux priors from land-surface models such as CASA may be highly uncertain.

777 **3.3 Spatial structure of model observation mismatch**

778 Spatial analysis of model-observation mismatch through experimental variograms
779 (Figure 8), confirms the previously reported findings. CT and WRF show similar struc-
780 tural behavior for LFT and HFT, while substantial differences emerge within the atmo-
781 spheric boundary layer. We determine the spatial extent of mismatch correlations (var-
782 iogram range) to be between 300 and 600 km (LFT: 267 and 309 km for CT and WRF
783 respectively; HFT: 405 and 576 km). The corresponding variances (variogram sill) are
784 for LFT 1.11 and 1.43 ppm² for CT and WRF, respectively as well as 0.48 and 0.62 ppm²
785 for HFT. In the ABL, the range is estimated 356 km for CT and 693 km for WRF, while
786 corresponding sills are 13.10 and 36.60 ppm². Note, however, that these values are highly
787 uncertain as we find generally large variability of model-data mismatches, as indicated
788 by the shading in Figure 8, compared to the average variogram. Also, we have compar-
789 atively little data that extended beyond 300 km as indicated by the drop in variance, due
790 to the inherent limitations of airborne data collection. Therefore, larger magnitude val-
791 ues for range as encountered in the ABL and WRF particularly are associated with larger
792 uncertainties in the fitting of the experimental variogram.

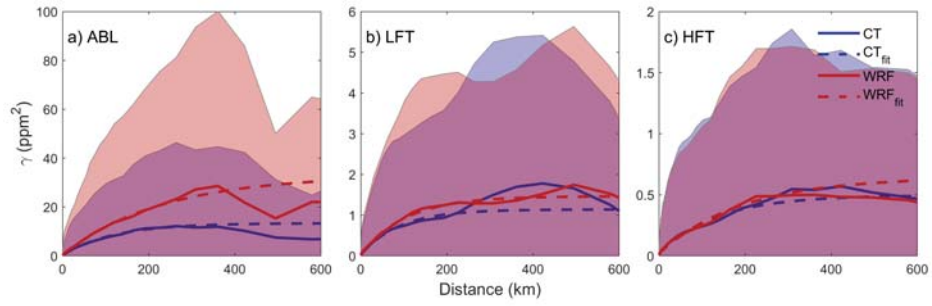


Figure 8. Experimental variogram for [CO₂] residuals for CT and WRF at levels (a) ABL; (b) LFT; and (c) HFT. The dashed lines indicate an exponential variogram fit. Shaded areas show the standard-deviation within each bin of the experimental variogram.

793 Overall, the mean spatial variance (γ) is small compared to the variability of model
794 data residuals (shading in Figure 8). Unfortunately, despite ACT’s more than 400,000
795 observations, we were not able to differentiate variogram statistics for season, region, and
796 air mass. We hypothesize that this is due to lack of observations at large distances that
797 preclude robust calculations of range and sill.

798 Recently, Lauvaux et al. (2019) investigated spatial error structures of in situ $[\text{CO}_2]$
799 from tower observations and found characteristic length scales (L) of order 100–150 km
800 during using a simple exponential ($e^{-x/L}$). Since the range of experimental variograms
801 is assumed to be $3 \times L$, we find our airborne observations comparable to the values given
802 by Lauvaux et al. (2019). Characteristic length-scales of order 100 km imply that $[\text{CO}_2]$
803 observations at the NOAA GML tall tower network (Andrews et al., 2014) are indepen-
804 dent of each other, while sufficient averaging lengths should be applied to satellite XCO_2
805 measurements.

806 3.4 Additional considerations

807 Our results show distinct $[\text{CO}_2]$ biases when observations are segregated by air mass.
808 Consequently, model evaluations, as commonly done, that average across different syn-
809 optic conditions are likely to hide canceling biases. Also, many observational systems,
810 such as satellites (e.g. OCO-2, Crowell et al., 2019) and the NOAA aircraft profiling ef-
811 forts (Sweeney et al., 2015) selectively sample fair weather conditions, which are were
812 found to be less biased. Resulting evaluations of model-data mismatch may thus under-
813 estimate the magnitude of transport model bias.

814 Biases related to air mass are likely linked to systematic differences in atmospheric
815 transport and the systematic differences in representation of weather system $[\text{CO}_2]$, found
816 in this work, may propagate to global meridional transport of $[\text{CO}_2]$. They therefore may
817 significantly affect global $[\text{CO}_2]$ inversion estimates as illustrated by Schuh et al. (2019)
818 and Barnes et al. (2016). Additional numerical studies and model-data comparisons should
819 be undertaken to quantify this link.

820 The importance of simulated transport on model-data mismatch is further high-
821 lighted by the fact that CT and WRF biases are of opposite sign, despite common car-
822 bon surface fluxes. Similarly, we find differences between CT and WRF with respect to
823 modeled cross frontal $[\text{CO}_2]$ differences, especially during Summer when WRF over-predicts

824 differences while CT tends to under-predict. The exact cause of this difference between
825 models, which will affect CO₂ transport in synoptic systems (Pal et al., 2020) is currently
826 unclear. Our results show that ABL depth alone cannot account for reported differences.
827 Potential causes may include resolved vertical transport and parameterized cloud mass
828 flux (Parazoo et al., 2008).

829 Magnitudes of model-data residuals strongly depend on air mass history and specif-
830 ically travel time over land (Sweeney et al., 2015; Lan et al., 2017) during which air parcels
831 are subject to CO₂ exchange with the biosphere. For example, warm sector air masses
832 originating from the south have less fetch over land compared to cold sector air masses
833 from the north. Therefore, southern air originating from the Gulf of Mexico provides a
834 homogeneous CO₂ background and thus less deviation from oceanic backgrounds, while
835 northern air masses that traveled through areas of large biospheric carbon fluxes such as
836 the Mid-West agricultural belt or boreal forests have much more varied [CO₂]. This high-
837 lights the importance of air mass history and transport error for model-observation mis-
838 match. While our work points to transport error differences as one source of the model-
839 data mismatch difference between warm and cold air masses, a true segregation of trans-
840 port from flux errors will likely require calibrated transport ensembles (Díaz-Isaac et al.,
841 2019; Feng, Lauvaux, Keller, et al., 2019; Feng, Lauvaux, Davis, et al., 2019).

842 Considering this work as a naive and uncalibrated 2-member model-ensemble, we
843 find seasonally varying model-model differences of 1–10 ppm. Within this range larger
844 differences pertain to warm and cold air masses, while smaller differences pertain to fair
845 weather conditions. Unfortunately, model-model differences are in the same range as com-
846 parisons with ACT observations, such that attribution of transport errors from our work
847 appears to be not possible, thus necessitating more targeted modeling studies.

848 In comparison to ABL [CO₂] residuals, residuals in the free troposphere were much
849 lower (< 0.5 ppm in HFT) and differences between CT and WRF were small, implying
850 that transport model errors were less important. Therefore, CO₂ observations in the higher
851 free troposphere may in many cases serve as continental background for greenhouse gas
852 measurements (e.g. Baier et al., 2020).

4 Conclusions

We use more than 400,000 CO₂ dry mole fraction observations collected during four flight campaigns spanning all four seasons and three regions (Northeast Mid-Atlantic, Mid-West, South-Central) in the Eastern U.S. to investigate model-observation mismatches for the WRF-Chem regional model and the global CarbonTracker system. A particular focus of this investigation and the ACT-America project in general, were synoptically active conditions, which present a major component of mid-latitude CO₂ transport and thus have the potential to greatly impact CO₂ inversion results.

Using identical carbon surface fluxes, we found that both models were capable of reproducing the [CO₂] dynamics over the Eastern U.S. At the same time, model-model mismatches and model observation mismatches were found to be strongly related to season and airmass, with synoptically active conditions and seasons to exhibit higher bias than fair weather conditions.

While errors in CT posterior fluxes likely play a considerable role in model-observation mismatch, we also qualitatively identified CO₂ transport as a major component, because the CT exhibited negative bias, while WRF had positive bias, despite common fluxes. However, it was not possible to quantify the magnitude of transport error, which was found to be due to horizontal transport rather than boundary-layer depth errors alone. While the two models used in this study could be considered a naive 2-member ensemble, further studies using carefully assembled model ensembles are needed to characterize transport uncertainty. Better quantification of transport uncertainty and improvements to transport models has the potential to improve inversion efforts as currently observations may be overly discounted in inversion products.

Comparing the lower resolution and global CT system with the WRF regional model, we find that while CT was capable of reproducing the principal [CO₂] dynamics associated with synoptic scale systems, WRF's higher resolution showed a clearer distinction between [CO₂] residuals in warm and cold airmasses. Given the stark cross frontal [CO₂] differences and the overall importance of weather systems for CO₂ transport, there is a likely benefit to making transport errors in inversion systems weather aware. This idea also highlights the potential of regional inversion systems to improve posterior carbon flux estimates. At the same time, caution should be taken because residual distributions were highly non-Gaussian and long-tailed and the higher resolution WRF-model

885 had heavier tails than CT, such that the assumption of Gaussian errors in regional in-
886 version systems lead to a further discounting of observational evidence due to overesti-
887 mation of transport errors.

888 In contrast to considerable model biases in the atmospheric boundary-layer we only
889 found small biases in the free troposphere and only small differences between models,
890 highlighting the fact that upper tropospheric measurements of CO₂ may be suitable for
891 characterizing continental CO₂ background conditions, which would improve our abil-
892 ity to investigate near surface.

893 In summary, our work demonstrated the utility of using ACT airborne [CO₂] mea-
894 surements to investigate CO₂ model-observation mismatch across seasons, regions, and
895 airmass conditions and provide a pathway for similar investigations using targeted model
896 ensembles and to identify the processes responsible for model-observation mismatch.

897 **Acknowledgments**

898 Observational data is available from the ACT public data repository hosted
899 by Oak Ridge National Lab. This work uses the *ACT-America: L3 Merged In Situ*
900 *Atmospheric Trace Gases and Flask Data, Eastern USA* (Davis et al., 2018). WRF
901 simulation for ACT-America (Feng et al., 2020) are available at The Pennsylvania
902 State University Data Commons. CarbonTracker CT2017 and CT-NRT.v2019-2
903 results are provided by NOAA ESRL, Boulder, Colorado, USA from the website
904 at <http://carbontracker.noaa.gov>. The use of NOAA's Observation Package (OB-
905 SPACK) for CT2017 and CT-NRT-2019.2 downloaded from the ObsPack Data
906 Portal at www.esrl.noaa.gov/gmd/ccgg/obspack/ is acknowledged. The Atmo-
907 spheric Carbon and Transport-America (ACT) project was sponsored by the Na-
908 tional Aeronautics and Space Administration (NASA) under awards NNX15AG76G
909 and NNX15AJ06G. T. Lauvaux was also supported by the French research pro-
910 gram Make Our Planet Great Again (Project CIUDAD - CNRS). We thank NASA's
911 Airborne Sciences program, NASA Headquarters and staff, in particular, Kenneth
912 W. Jucks and Jennifer R. Olson for their support of our mission. We would like to
913 acknowledge the contributions of ACT collaborators, in particular, NASA project
914 managers, scientists, and engineers and our colleagues at NOAA, Colorado State
915 University for their excellent cooperation during the field campaign. Thanks are

916 also due to the flight crews and aircraft facility groups from Wallops Flight Facility,
917 Langley Research Center, and Duncan Aviation for their outstanding work sup-
918 porting these flights and measurements. We also thank Hannah Halliday and John
919 B. Novack for their contributions in data collection.

920 **References**

- 921 Agustí-Panareda, A., Diamantakis, M., Massart, S., Chevallier, F., Muñoz-Sabater,
 922 J., Barré, J., . . . Wunch, D. (2019). Modelling CO₂ weather – why horizontal
 923 resolution matters. *Atmospheric Chemistry and Physics*, *19*(11), 7347–7376.
 924 doi: 10.5194/acp-19-7347-2019
- 925 Andres, R. J., Gregg, J. S., Losey, L., Marland, G., & Boden, T. A. (2011).
 926 Monthly, global emissions of carbon dioxide from fossil fuel consump-
 927 tion. *Tellus B: Chemical and Physical Meteorology*, *63*(3), 309–327. doi:
 928 10.1111/j.1600-0889.2011.00530.x
- 929 Andrews, A. E., Kofler, J. D., Trudeau, M. E., Williams, J. C., Neff, D. H., Masarie,
 930 K. A., . . . Tans, P. P. (2014). CO₂, CO, and CH₄ measurements from tall tow-
 931 ers in the NOAA Earth System Research Laboratory’s Global Greenhouse Gas
 932 Reference Network: Instrumentation, uncertainty analysis, and recommenda-
 933 tions for future high-accuracy greenhouse gas monitoring efforts. *Atmospheric*
 934 *Measurement Techniques*, *7*(2), 647–687. doi: 10.5194/amt-7-647-2014
- 935 Baier, B. C., Sweeney, C., Choi, Y., Davis, K. J., DiGangi, J. P., Feng, S., . . . Weib-
 936 ring, P. (2020). Multispecies assessment of factors influencing regional CO₂
 937 and CH₄ enhancements during the winter 2017 ACT-America campaign. *Jour-*
 938 *nal of Geophysical Research: Atmospheres*, *125*(2), e2019JD031339. doi:
 939 10.1029/2019JD031339
- 940 Baker, D. F., Doney, S. C., & Schimel, D. S. (2006). Variational data assimilation
 941 for atmospheric CO₂. *Tellus B: Chemical and Physical Meteorology*, *58*(5),
 942 359–365. doi: 10.1111/j.1600-0889.2006.00218.x
- 943 Barnes, E. A., Parazoo, N., Orbe, C., & Denning, A. S. (2016). Isentropic transport
 944 and the seasonal cycle amplitude of CO₂. *Journal of Geophysical Research: At-*
 945 *mospheres*, *121*(13), 8106–8124. doi: 10.1002/2016JD025109
- 946 Basu, S., Baker, D. F., Chevallier, F., Patra, P. K., Liu, J., & Miller, J. B. (2018).
 947 The impact of transport model differences on CO₂ surface flux estimates from
 948 OCO-2 retrievals of column average CO₂. *Atmospheric Chemistry and Physics*,
 949 *18*(10), 7189–7215. doi: 10.5194/acp-18-7189-2018
- 950 Blasing, T. J., Broniak, C. T., & Marland, G. (2005). The annual cycle of fossil-fuel
 951 carbon dioxide emissions in the United States. *Tellus B: Chemical and Physi-*
 952 *cal Meteorology*, *57*(2), 107–115. doi: 10.3402/tellusb.v57i2.16779

- 953 Boden, T., Andres, R., & Marland, G. (2016). *Global, Regional, and National*
 954 *Fossil-Fuel CO₂ Emissions (1751 - 2013) (V. 2016)*. Environmental System
 955 Science Data Infrastructure for a Virtual Ecosystem; Carbon Dioxide Informa-
 956 tion Analysis Center (CDIAC), Oak Ridge National Laboratory (ORNL), Oak
 957 Ridge, TN (United States). doi: 10.3334/CDIAC/00001_V2016
- 958 Bousquet, P., Ciais, P., Peylin, P., Ramonet, M., & Monfray, P. (1999). Inverse
 959 modeling of annual atmospheric CO₂ sources and sinks: 1. Method and con-
 960 trol inversion. *Journal of Geophysical Research: Atmospheres*, *104*(D21),
 961 26161–26178. doi: 10.1029/1999JD900342
- 962 Butler, M. P., Lauvaux, T., Feng, S., Liu, J., Bowman, K. W., & Davis, K. J.
 963 (2020). Atmospheric simulations of total column CO₂ mole fractions from
 964 global to mesoscale within the Carbon Monitoring System Flux Inversion
 965 Framework. *Atmosphere*, *11*(8), 787. doi: 10.3390/atmos11080787
- 966 Chan, D., Yuen, C. W., Higuchi, K., Shashkov, A., Liu, J., Chen, J., & Worthy, D.
 967 (2004). On the CO₂ exchange between the atmosphere and the biosphere: The
 968 role of synoptic and mesoscale processes. *Tellus B: Chemical and Physical*
 969 *Meteorology*, *56*(3), 194–212. doi: 10.3402/tellusb.v56i3.16424
- 970 Chen, H. W., Zhang, F., Lauvaux, T., Davis, K. J., Feng, S., Butler, M., & Alley,
 971 R. B. (2019). Characterization of regional-scale CO₂ transport uncertainties
 972 in an ensemble with flow-dependent transport errors. *Geophysical Research*
 973 *Letters*, *46*(7), 4049–4058. doi: 10.1029/2018GL081341
- 974 Chen, H. W., Zhang, L. N., Zhang, F., Davis, K. J., Lauvaux, T., Pal, S., . . . Di-
 975 Gangi, J. P. (2019). Evaluation of regional CO₂ mole fractions in the ECMWF
 976 CAMS real-time atmospheric analysis and NOAA CarbonTracker Near-Real-
 977 Time reanalysis with airborne observations from ACT-America field cam-
 978 paigns. *Journal of Geophysical Research: Atmospheres*, *124*(14), 8119–8133.
 979 doi: 10.1029/2018JD029992
- 980 Chevallier, F., Feng, L., Bösch, H., Palmer, P. I., & Rayner, P. J. (2010). On the
 981 impact of transport model errors for the estimation of CO₂ surface fluxes
 982 from GOSAT observations. *Geophysical Research Letters*, *37*(21). doi:
 983 10.1029/2010GL044652
- 984 Ciais, P., Sabine, C., Bala, G., Bopp, L., Brovkin, V., Canadell, J., . . . Thornton,
 985 P. E. (2013). Carbon and other biogeochemical cycles. In *Climate Change*

- 986 2013: *The Physical Science Basis. Contribution of Working Group I to the*
987 *Fifth Assessment Report of the Intergovernmental Panel on Climate Change*
988 (pp. 465–570). Cambridge, UK; New York, USA: Cambridge University Press.
- 989 Comission, E. (2019). *Emissions Database for Global Atmospheric Research*
990 (*EDGAR*).
- 991 Crowell, S., Baker, D., Schuh, A., Basu, S., Jacobson, A. R., Chevallier, F., ...
992 Jones, D. B. A. (2019). The 2015–2016 carbon cycle as seen from OCO-2
993 and the global in situ network. *Atmospheric Chemistry and Physics*, 19(15),
994 9797–9831. doi: 10.5194/acp-19-9797-2019
- 995 Davis, K., Obland, M., Lin, B., Lauvvaux, T., O’Dell, C., Meadows, B., ... Nehrir,
996 A. (2018). *ACT-America: L3 Merged In Situ Atmospheric Trace Gases and*
997 *Flask Data, Eastern USA*. ORNL Distributed Active Archive Center. doi:
998 10.3334/ORNLDAAC/1593
- 999 Denning, A. S., Fung, I. Y., & Randall, D. (1995). Latitudinal gradient of atmo-
1000 spheric CO₂ due to seasonal exchange with land biota. *Nature*, 376(6537), 240.
1001 doi: 10.1038/376240a0
- 1002 Díaz-Isaac, L. I., Lauvvaux, T., Bocquet, M., & Davis, K. J. (2019). Calibration of
1003 a multi-physics ensemble for estimating the uncertainty of a greenhouse gas
1004 atmospheric transport model. *Atmospheric Chemistry and Physics*, 19(8),
1005 5695–5718. doi: 10.5194/acp-19-5695-2019
- 1006 Díaz-Isaac, L. I., Lauvvaux, T., & Davis, K. J. (2018). Impact of physical param-
1007 eterizations and initial conditions on simulated atmospheric transport and
1008 CO₂ mole fractions in the US Midwest. *Atmospheric Chemistry and Physics*,
1009 18(20), 14813–14835. doi: 10.5194/acp-18-14813-2018
- 1010 Díaz-Isaac, L. I., Lauvvaux, T., Davis, K. J., Miles, N. L., Richardson, S. J., Jacob-
1011 son, A. R., & Andrews, A. E. (2014). Model-data comparison of MCI field
1012 campaign atmospheric CO₂ mole fractions. *Journal of Geophysical Research:*
1013 *Atmospheres*, 119(17), 10536–10551. doi: 10.1002/2014JD021593
- 1014 Fast, J. D., Gustafson, W. I., Easter, R. C., Zaveri, R. A., Barnard, J. C., Chap-
1015 man, E. G., ... Peckham, S. E. (2006). Evolution of ozone, particulates, and
1016 aerosol direct radiative forcing in the vicinity of Houston using a fully cou-
1017 pled meteorology-chemistry-aerosol model. *Journal of Geophysical Research:*
1018 *Atmospheres*, 111(D21). doi: 10.1029/2005JD006721

- 1019 Feng, S., Lauvaux, T., Barkley, Z., Davis, K., Butler, M., Deng, A., . . . Stauffer, D.
 1020 (2020). *Full WRF-Chem output in support of the NASA Atmospheric Carbon*
 1021 *and Transport (ACT)-America project (7/1/2016 – 7/31/2019)*. Penn State
 1022 Data Commons. doi: 10.26208/RQF5-Q142
- 1023 Feng, S., Lauvaux, T., Davis, K. J., Keller, K., Zhou, Y., Williams, C., . . . Baker,
 1024 I. (2019). Seasonal characteristics of model uncertainties from biogenic fluxes,
 1025 transport, and large-scale boundary inflow in atmospheric CO₂ simulations
 1026 over North America. *Journal of Geophysical Research: Atmospheres*, *124*(24),
 1027 14325–14346. doi: 10.1029/2019JD031165
- 1028 Feng, S., Lauvaux, T., Keller, K., Davis, K. J., Rayner, P., Oda, T., & Gurney,
 1029 K. R. (2019). A road map for improving the treatment of uncertainties in
 1030 high-resolution regional carbon flux inverse estimates. *Geophysical Research*
 1031 *Letters*, *46*(22), 13431–13469. doi: 10.1029/2019GL082987
- 1032 Friedlingstein, P., Meinshausen, M., Arora, V. K., Jones, C. D., Anav, A., Lid-
 1033 dicoat, S. K., & Knutti, R. (2014). Uncertainties in CMIP5 Climate Pro-
 1034 jections due to Carbon Cycle Feedbacks. *J. Climate*, *27*(2), 511–526. doi:
 1035 10.1175/JCLI-D-12-00579.1
- 1036 Gaubert, B., Stephens, B. B., Basu, S., Chevallier, F., Deng, F., Kort, E. A., . . .
 1037 Yin, Y. (2019). Global atmospheric CO₂ inverse models converging on neutral
 1038 tropical land exchange, but disagreeing on fossil fuel and atmospheric growth
 1039 rate. *Biogeosciences*, *16*(1), 117–134. doi: 10.5194/bg-16-117-2019
- 1040 Geels, C., Gloor, M., Ciais, P., Bousquet, P., Peylin, P., Vermeulen, A. T., . . .
 1041 Santaguida, R. (2007). Comparing atmospheric transport models for fu-
 1042 ture regional inversions over Europe – Part 1: Mapping the atmospheric
 1043 CO₂ signals. *Atmospheric Chemistry and Physics*, *7*(13), 3461–3479. doi:
 1044 10.5194/acp-7-3461-2007
- 1045 Gerbig, C., Körner, S., & Lin, J. C. (2008). Vertical mixing in atmospheric tracer
 1046 transport models: Error characterization and propagation. *Atmospheric Chem-*
 1047 *istry and Physics*, *8*(3), 591–602. doi: 10.5194/acp-8-591-2008
- 1048 Gerken, T. (2019, May). *TobGerken/ACT_ManueverFlags V1.0*. Zenodo. doi: 10
 1049 .5281/zenodo.2677933
- 1050 Giglio, L., Loboda, T., Roy, D. P., Quayle, B., & Justice, C. O. (2009). An active-
 1051 fire based burned area mapping algorithm for the MODIS sensor. *Remote*

- 1052 *Sensing of Environment*, 113(2), 408–420. doi: 10.1016/j.rse.2008.10.006
- 1053 Giglio, L., Randerson, J. T., & van der Werf, G. R. (2013). Analysis of daily,
1054 monthly, and annual burned area using the fourth-generation global fire emis-
1055 sions database (GFED4). *Journal of Geophysical Research: Biogeosciences*,
1056 118(1), 317–328. doi: 10.1002/jgrg.20042
- 1057 Gourdj, S. M., Mueller, K. L., Yadav, V., Huntzinger, D. N., Andrews, A. E.,
1058 Trudeau, M., . . . Michalak, A. M. (2012). North American CO₂ exchange:
1059 Inter-comparison of modeled estimates with results from a fine-scale atmo-
1060 spheric inversion. *Biogeosciences*, 9(1), 457–475. doi: 10.5194/bg-9-457-2012
- 1061 Grell, G. A., Peckham, S. E., Schmitz, R., McKeen, S. A., Frost, G., Skamarock,
1062 W. C., & Eder, B. (2005). Fully coupled “online” chemistry within
1063 the WRF model. *Atmospheric Environment*, 39(37), 6957–6975. doi:
1064 10.1016/j.atmosenv.2005.04.027
- 1065 Gurney, K. R., Law, R. M., Denning, A. S., Rayner, P. J., Baker, D., Bousquet, P.,
1066 . . . Yuen, C.-W. (2002). Towards robust regional estimates of CO₂ sources
1067 and sinks using atmospheric transport models. *Nature*, 415(6872), 626. doi:
1068 10.1038/415626a
- 1069 Hu, L., Andrews, A. E., Thoning, K. W., Sweeney, C., Miller, J. B., Michalak,
1070 A. M., . . . van der Velde, I. R. (2019). Enhanced North American carbon
1071 uptake associated with El Niño. *Science Advances*, 5(6), eaaw0076. doi:
1072 10.1126/sciadv.aaw0076
- 1073 Huntzinger, D. N., Post, W. M., Wei, Y., Michalak, A. M., West, T. O., Jacob-
1074 son, A. R., . . . Cook, R. (2012). North American Carbon Program (NACP)
1075 regional interim synthesis: Terrestrial biospheric model intercomparison. *Eco-*
1076 *logical Modelling*, 232, 144–157. doi: 10.1016/j.ecolmodel.2012.02.004
- 1077 Jacobson, A. R., Fletcher, S. E. M., Gruber, N., Sarmiento, J. L., & Gloor, M.
1078 (2007). A joint atmosphere-ocean inversion for surface fluxes of carbon dioxide:
1079 1. Methods and global-scale fluxes. *Global Biogeochemical Cycles*, 21(1). doi:
1080 10.1029/2005GB002556
- 1081 Keppel-Aleks, G., Wennberg, P. O., & Schneider, T. (2011). Sources of variations
1082 in total column carbon dioxide. *Atmospheric Chemistry and Physics*, 11(8),
1083 3581–3593. doi: 10.5194/acp-11-3581-2011
- 1084 Keppel-Aleks, G., Wennberg, P. O., Washenfelder, R. A., Wunch, D., Schneider,

- 1085 T., Toon, G. C., . . . Wofsy, S. C. (2012). The imprint of surface fluxes and
1086 transport on variations in total column carbon dioxide. *Biogeosciences*, *9*(3),
1087 875–891. doi: 10.5194/bg-9-875-2012
- 1088 Krol, M., Houweling, S., Bregman, B., van den Broek, M., Segers, A., van Velthoven,
1089 P., . . . Bergamaschi, P. (2005). The two-way nested global chemistry-transport
1090 zoom model TM5: Algorithm and applications. *Atmospheric Chemistry and*
1091 *Physics*, *5*(2), 417–432. doi: 10.5194/acp-5-417-2005
- 1092 Lan, X., Tans, P., Sweeney, C., Andrews, A., Jacobson, A., Crotnell, M., . . . Wolter,
1093 S. (2017). Gradients of column CO₂ across North America from the NOAA
1094 Global Greenhouse Gas Reference Network. *Atmospheric Chemistry and*
1095 *Physics*, *17*(24), 15151–15165. doi: 10.5194/acp-17-15151-2017
- 1096 Lauvaux, T., & Davis, K. J. (2014). Planetary boundary layer errors in mesoscale
1097 inversions of column-integrated CO₂ measurements. *Journal of Geophysical*
1098 *Research: Atmospheres*, *119*(2), 490–508. doi: 10.1002/2013JD020175
- 1099 Lauvaux, T., Díaz-Isaac, L. I., Bocquet, M., & Bousserez, N. (2019). Diagnos-
1100 ing spatial error structures in CO₂ mole fractions and XCO₂ column mole
1101 fractions from atmospheric transport. *Atmospheric Chemistry and Physics*,
1102 *19*(18), 12007–12024. doi: 10.5194/acp-19-12007-2019
- 1103 Lauvaux, T., Schuh, A. E., Bocquet, M., Wu, L., Richardson, S., Miles, N., & Davis,
1104 K. J. (2012). Network design for mesoscale inversions of CO₂ budget of the
1105 corn belt: Exploring uncertainty sources and sinks. *Tellus B: Chemical and*
1106 *Physical Meteorology*, *64*(1), 17980. doi: 10.3402/tellusb.v64i0.17980
- 1107 Lauvaux, T., Schuh, A. E., Uliasz, M., Richardson, S., Miles, N., Andrews, A. E., . . .
1108 Davis, K. J. (2012). Constraining the CO₂ budget of the corn belt: Exploring
1109 uncertainties from the assumptions in a mesoscale inverse system. *Atmospheric*
1110 *Chemistry and Physics*, *12*(1), 337–354. doi: 10.5194/acp-12-337-2012
- 1111 Masarie, K. A., Peters, W., Jacobson, A. R., & Tans, P. P. (2014). ObsPack: A
1112 framework for the preparation, delivery, and attribution of atmospheric green-
1113 house gas measurements. *Earth System Science Data*, *6*(2), 375–384. doi:
1114 10.5194/essd-6-375-2014
- 1115 Matheron, G. (1963). Principles of geostatistics. *Economic Geology*, *58*(8), 1246–
1116 1266. doi: 10.2113/gsecongeo.58.8.1246
- 1117 Merrill, J. T., & Moody, J. L. (1996). Synoptic meteorology and transport during

- 1118 the North Atlantic Regional Experiment (NARE) intensive: Overview. *Journal*
 1119 *of Geophysical Research: Atmospheres*, 101(D22), 28903–28921. doi: 10.1029/
 1120 96JD00097
- 1121 Myhre, G., Shindell, D. T., Breon, F.-M., Collins, W., Fuglestedt, J., Huang, J.,
 1122 ... Zhang, H. (2013). Anthropogenic and Natural Radiative Forcing. In *Cli-*
 1123 *mate Change 2013 - The Physical Science Basis* (pp. 659–740). Cambridge:
 1124 Cambridge University Press. doi: 10.1017/CBO9781107415324.018
- 1125 Nassar, R., Napier-Linton, L., Gurney, K. R., Andres, R. J., Oda, T., Vogel, F. R.,
 1126 & Deng, F. (2013). Improving the temporal and spatial distribution of CO₂
 1127 emissions from global fossil fuel emission data sets. *Journal of Geophysical*
 1128 *Research: Atmospheres*, 118(2), 917–933. doi: 10.1029/2012JD018196
- 1129 Oda, T., & Maksyutov, S. (2011). A very high-resolution (1 km x 1 km) global fossil
 1130 fuel CO₂ emission inventory derived using a point source database and satellite
 1131 observations of nighttime lights. *Atmospheric Chemistry and Physics*, 11(2),
 1132 543–556. doi: 10.5194/acp-11-543-2011
- 1133 Olsen, S. C., & Randerson, J. T. (2004). Differences between surface and column
 1134 atmospheric CO₂ and implications for carbon cycle research. *Journal of Geo-*
 1135 *physical Research: Atmospheres*, 109(D2). doi: 10.1029/2003JD003968
- 1136 Pal, S., Davis, K. J., Lauvaux, T., Browell, E. V., Gaudet, B. J., Stauffer, D. R.,
 1137 ... Zhang, F. (2020). Observations of greenhouse gas changes across summer
 1138 frontal boundaries in the eastern United States. *J. Geophys. Res. Atmos.*, 125,
 1139 e2019JD030526. doi: 10.1029/2019JD030526
- 1140 Parazoo, N. C., Denning, A. S., Berry, J. A., Wolf, A., Randall, D. A., Kawa,
 1141 S. R., ... Doney, S. C. (2011). Moist synoptic transport of CO₂ along
 1142 the mid-latitude storm track. *Geophysical Research Letters*, 38(9). doi:
 1143 10.1029/2011GL047238
- 1144 Parazoo, N. C., Denning, A. S., Kawa, S. R., Corbin, K. D., Lokupitiya, R. S., &
 1145 Baker, I. T. (2008). Mechanisms for synoptic variations of atmospheric CO₂
 1146 in North America, South America and Europe. *Atmospheric Chemistry and*
 1147 *Physics*, 8(23), 7239–7254. doi: 10.5194/acp-8-7239-2008
- 1148 Parazoo, N. C., Denning, A. S., Kawa, S. R., Pawson, S., & Lokupitiya, R. (2012).
 1149 CO₂ flux estimation errors associated with moist atmospheric processes. *Atmo-*
 1150 *spheric Chemistry and Physics*, 12(14), 6405–6416. doi: 10.5194/acp-12-6405

- 1151 -2012
- 1152 Patton, A., Politis, D. N., & White, H. (2009). Correction to “Automatic block-
- 1153 length selection for the dependent bootstrap” by D. Politis and H. White.
- 1154 *Econometric Reviews*, *28*(4), 372–375. doi: 10.1080/07474930802459016
- 1155 Peters, W., Jacobson, A. R., Sweeney, C., Andrews, A. E., Conway, T. J., Masarie,
- 1156 K., . . . Tans, P. P. (2007). An atmospheric perspective on North American
- 1157 carbon dioxide exchange: CarbonTracker. *PNAS*, *104*(48), 18925–18930. doi:
- 1158 10.1073/pnas.0708986104
- 1159 Peylin, P., Law, R. M., Gurney, K. R., Chevallier, F., Jacobson, A. R., Maki, T.,
- 1160 . . . Zhang, X. (2013). Global atmospheric carbon budget: Results from an
- 1161 ensemble of atmospheric CO₂ inversions. *Biogeosciences*, *10*(10), 6699–6720.
- 1162 doi: 10.5194/bg-10-6699-2013
- 1163 Peylin, P., Rayner, P. J., Bousquet, P., Carouge, C., Hourdin, F., Heinrich, P., . . .
- 1164 AEROCARB contributors (2005). Daily CO₂ flux estimates over Europe from
- 1165 continuous atmospheric measurements: 1. Inverse methodology. *Atmospheric*
- 1166 *Chemistry and Physics*, *5*(12), 3173–3186. doi: 10.5194/acp-5-3173-2005
- 1167 Politis, D. N., & White, H. (2004). Automatic block-length selection for the de-
- 1168 pendent bootstrap. *Econometric Reviews*, *23*(1), 53–70. doi: 10.1081/ETC
- 1169 -120028836
- 1170 Potter, C. S., Klooster, S. A., Myneni, R., Genovese, V., Tan, P.-N., & Kumar, V.
- 1171 (2003). Continental-scale comparisons of terrestrial carbon sinks estimated
- 1172 from satellite data and ecosystem modeling 1982–1998. *Global and Planetary*
- 1173 *Change*, *39*(3), 201–213. doi: 10.1016/j.gloplacha.2003.07.001
- 1174 Potter, C. S., Randerson, J. T., Field, C. B., Matson, P. A., Vitousek, P. M.,
- 1175 Mooney, H. A., & Klooster, S. A. (1993). Terrestrial ecosystem production: A
- 1176 process model based on global satellite and surface data. *Global Biogeochemical*
- 1177 *Cycles*, *7*(4), 811–841. doi: 10.1029/93GB02725
- 1178 Powers, J. G., Klemp, J. B., Skamarock, W. C., Davis, C. A., Dudhia, J., Gill,
- 1179 D. O., . . . Duda, M. G. (2017). The Weather Research and Forecasting Model:
- 1180 Overview, system efforts, and future directions. *Bull. Amer. Meteor. Soc.*,
- 1181 *98*(8), 1717–1737. doi: 10.1175/BAMS-D-15-00308.1
- 1182 Rasmussen, L. A. (1991). Piecewise integral splines of low degree. *Computers &*
- 1183 *Geosciences*, *17*(9), 1255–1263. doi: 10.1016/0098-3004(91)90027-B

- 1184 Schuh, A. E., Jacobson, A. R., Basu, S., Weir, B., Baker, D., Bowman, K., ...
 1185 Palmer, P. I. (2019). Quantifying the impact of atmospheric transport un-
 1186 certainty on CO₂ surface flux estimates. *Global Biogeochemical Cycles*, *33*(4),
 1187 484–500. doi: 10.1029/2018GB006086
- 1188 Schuh, A. E., Lauvaux, T., West, T. O., Denning, A. S., Davis, K. J., Miles, N., ...
 1189 Ogle, S. (2013). Evaluating atmospheric CO₂ inversions at multiple scales
 1190 over a highly inventoried agricultural landscape. *Glob Change Biol*, *19*(5),
 1191 1424–1439. doi: 10.1111/gcb.12141
- 1192 Schwanghart, W. (2013). *Experimental (Semi-) Variogram Version 1.4.0*.
 1193 [https://www.mathworks.com/matlabcentral/fileexchange/20355-experimental-](https://www.mathworks.com/matlabcentral/fileexchange/20355-experimental-semi-variogram)
 1194 [semi-variogram](https://www.mathworks.com/matlabcentral/fileexchange/20355-experimental-semi-variogram).
- 1195 Skamarock, W. C., Klemp, J., Dudhia, J., Gill, D., Barker, D., Wang, W., ... Duda,
 1196 M. (2008). *A Description of the Advanced Research WRF Version 3* (Tech.
 1197 Rep.). UCAR/NCAR. doi: 10.5065/D68S4MVH
- 1198 Stephens, B. B., Gurney, K. R., Tans, P. P., Sweeney, C., Peters, W., Bruhwiler, L.,
 1199 ... Denning, A. S. (2007). Weak northern and strong tropical land carbon up-
 1200 take from vertical profiles of atmospheric CO₂. *Science*, *316*(5832), 1732–1735.
 1201 doi: 10.1126/science.1137004
- 1202 Sweeney, C., Karion, A., Wolter, S., Newberger, T., Guenther, D., Higgs, J. A., ...
 1203 Tans, P. P. (2015). Seasonal climatology of CO₂ across North America from
 1204 aircraft measurements in the NOAA/ESRL Global Greenhouse Gas Reference
 1205 Network. *Journal of Geophysical Research: Atmospheres*, *120*(10), 5155–5190.
 1206 doi: 10.1002/2014JD022591
- 1207 Takahashi, T., Sutherland, S. C., Wanninkhof, R., Sweeney, C., Feely, R. A., Chip-
 1208 man, D. W., ... de Baar, H. J. W. (2009). Climatological mean and decadal
 1209 change in surface ocean pCO₂, and net sea–air CO₂ flux over the global
 1210 oceans. *Deep Sea Research Part II: Topical Studies in Oceanography*, *56*(8),
 1211 554–577. doi: 10.1016/j.dsr2.2008.12.009
- 1212 van der Werf, G. R., Randerson, J. T., Giglio, L., Collatz, G. J., Kasibhatla, P. S.,
 1213 & Arellano Jr., A. F. (2006). Interannual variability in global biomass burn-
 1214 ing emissions from 1997 to 2004. *Atmospheric Chemistry and Physics*, *6*(11),
 1215 3423–3441. doi: 10.5194/acp-6-3423-2006
- 1216 Wei, Y., Shresha, R., Pal, S., Gerken, T., McNelis, J., Singh, D., ... Davis, K. J. (in

1217

review). The ACT-America Datasets: Description, Management and Delivery.

1218

Earth and Space Sciences.